Article

Anti-Collision Path Planning and Tracking of Autonomous Vehicle Based on Optimized Artificial Potential Field and Discrete LQR Algorithm

Chaoxia Zhang [1], **Zhihao Chen** [1,*], **Xingjiao Li** [2] **and Ting Zhao** [1]

[1] School of Mechanicalan Electrical Engineering and Automation, Foshan University, Foshan 528225, China; chaoxia_zhang@163.com (C.Z.)
[2] Center of Teacher's Teaching Development, Guangdong University of Education, Guangzhou 510303, China
* Correspondence: 2112202057@stu.fosu.edu.cn

Abstract: This paper introduces an enhanced APF method to address challenges in automatic lane changing and collision avoidance for autonomous vehicles, targeting issues of infeasible target points, local optimization, inadequate safety margins, and instability when using DLQR. By integrating a distance adjustment factor, this research aims to rectify traditional APF limitations. A safety distance model and a sub-target virtual potential field are established to facilitate collision-free path generation for autonomous vehicles. A path tracking system is designed, combining feed-forward control with DLQR. Linearization and discretization of the vehicle's dynamic state space model, with constraint variables set to minimize control-command costs, aligns with DLQR objectives. The aim is precise steering angle determination for path tracking, negating lateral errors due to external disturbances. A Simulink–CarSim co-simulation platform is utilized for obstacle and speed scenarios, validating the autonomous vehicle's dynamic hazard avoidance, lane changing, and overtaking capabilities. The refined APF method enhances path safety, smoothness, and stability. Experimental data across three speeds reveal reasonable steering angle and lateral deflection angle variations. The controller ensures stable reference path tracking at 40, 50, and 60 km/h around various obstacles, verifying the controller's effectiveness and driving stability. Comparative analysis of visual trajectories pre-optimization and post-optimization highlights improvements. Vehicle roll and sideslip angle peaks, roll-angle fluctuation, and front/rear wheel steering vertical support forces are compared with traditional LQR, validating the optimized controller's enhancement of vehicle performance. Simulation results using MATLAB/Simulink and CarSim demonstrate that the optimized controller reduces steering angles by 5 to 10°, decreases sideslip angles by 3 to 5°, and increases vertical support forces from 1000 to 1450 N, showcasing our algorithm's superior obstacle avoidance and lane-changing capabilities under dynamic conditions.

Keywords: path planning; artificial potential field algorithms; collision avoidance; path tracking; linear quadratic optimal controller

1. Introduction

With the rapid advancements in computer science, technology, and artificial intelligence, the prospect of replacing human drivers with automated driving systems is becoming a reality. The development of autonomous driving has enabled people to progressively relinquish control to these systems [1]. The integration of the Internet of Things and artificial intelligence into vehicles has endowed them with their own decision-making capabilities. Consequently, intelligent autonomous driving technology is gradually assuming the role of the conventional "perception–decision–execution" process carried out by human drivers. A highly sophisticated product, autonomous driving integrates a number of cutting-edge technologies, such as environment sensing, decision-making, and following control systems. Autonomous driving systems (ADS), enhanced by sensor integration and innovative

vehicle features, spawn a rich array of benefits. Autonomous vehicles are able to plan routes and adjust driving styles more efficiently, for example, reducing sharp acceleration and braking, which in turn reduces fuel consumption and emissions. It is estimated that self-driving cars can reduce their carbon footprint by up to 90% compared to conventional vehicles. The combination of autonomous driving technology with new energy vehicles, such as electric vehicles (EVs) and hydrogen fuel cell vehicles (FCEVs), accelerates the shift toward green mobility solutions and further reduces fossil fuel dependence. Autonomous driving technology also offers seniors a new way to travel independently, safely, and easily to their destinations, even in the face of physical decline. This greatly improves their quality of life and social participation. As the elderly reintegrate into social activities, their consumption and employment potential is also activated, injecting new vitality into economic growth. Dudziak et al. [2] noted that the emergence of new technologies has facilitated the development and gradual implementation of autonomous vehicle (AV) concepts, catering to the demands of aging demographics in industrialized nations and establishing AVs as both a necessity and a viable business model. Autonomous vehicles employ sophisticated sensors and algorithms to adjust acceleration, deceleration, and cornering limits, enhancing passenger comfort by avoiding the jolts of sudden starts or stops. Hwang et al. [3] proposed a comfort regenerative braking system (CRBS) that utilizes artificial neural networks to control vehicle braking. The driving comfort of an autonomous vehicle primarily depends on its control algorithm. If the passenger's comfort is initially predicted based on acceleration and deceleration thresholds, the control strategy algorithm can be adjusted, which helps to improve the ride comfort of the autonomous vehicle. A numerical analysis of this control strategy demonstrated its effectiveness in reducing jolting conditions, verifying the CRBS's improvement over traditional braking systems. The proposed CRBS provided effective regenerative braking within the limits and ensured increased passenger driving comfort. Autonomous vehicles are equipped with sensors and advanced algorithms that can identify and react to hazards ahead of time, prevent potential collisions, and even proactively avoid hazards in emergency situations, dramatically improving driving safety. The cardinal benefit anticipated from advanced vehicle systems is the substantial abatement of both accident frequency and severity. Indeed, proponents of these technologies champion their potential to all but eliminate human error—an overarching factor in road mishaps. By leveraging automation and intelligent interventions, such systems target the very core of operational vulnerabilities and pave the way for a paradigm shift in traffic safety [4].

The paramount concern within the domain of vehicular safety pertains to collision prevention on our roads, encapsulated starkly by the grim tally of accidents and collisions [5]. It is projected that AVs hold significant potential to dramatically curtail mishaps attributable to human fallibility—such misjudgments currently constitute upwards of 90% of total vehicular incidents, encompassing distractions (e.g., smartphone usage), excessive velocity, impaired operation under intoxicants, fatigue, and impulsive judgments [6]. These advancements stand poised not only to precipitously decrease casualties but also to bolster emergency responsiveness. Notably, AVs outshine human operators in terms of inter-vehicular communication, boasting superior awareness of fellow road participants' whereabouts while accurately forecasting their movements. Moreover, they mitigate risks associated with drowsy driving [7]. Consequently, these autonomous marvels contribute to life preservation via state-of-the-art avoidance strategies coupled with enhanced crash mitigation protocols. Underpinning this capability lies their adeptness in monitoring the surrounding traffic milieu, charting courses via intricate software algorithms, and orchestrating vehicular maneuvers independently of direct human command. In essence, AVs harness cutting-edge detection capabilities, navigational prowess, and autonomous action to redefine vehicular safety standards, thereby heralding a new era of reduced accident rates and enhanced occupant security [8]. Path planning serves as the foundation of automatic driving, while path following is a crucial technology. By implementing reasonable path planning and accurate path tracking, road safety can be ensured, traffic accidents can be avoided, passenger comfort can be maintained, and traffic congestion can be reduced.

Path planning has received much attention in the study of obstacle avoidance for autonomous vehicles. Path design for self-driving automobiles must take into account regulations and road architecture, in addition to impediments. In order to make the planned path easier for the vehicle to follow, vehicle dynamics, as well as the constraints of the actuating controller, are taken into account at the path-planning level. Local path planning is a crucial technique for addressing the active safety issues with self-driving cars. Significant characteristics include excellent computing efficiency and real-time performance. The most common local path-planning algorithms currently include A*, genetic, ant colony, particle swarm, and artificial potential field (APF) methods. The potential field is created using the artificial potential field method based on the potential functions of objectives, road constructions, and barriers. It moves along the potential field's downward direction as it plans the route. The route tracking module then figures out the inputs needed from the vehicle to track the path. Its low computational cost, even for complicated path planning, including barriers and road features, is this method's key benefit over other path-planning approaches. It benefits from quick searches, tremendous computational power, and simple modeling. In contrast to other algorithms, the approach is also well suited for active obstacle avoidance in self-driving automobiles [9]. Using the conventional artificial potential field technique, the vehicular operating landscape is delineated; gravitational pulls and repulsions contour around impediments, constructing the environmental framework. The conventional APF-based vehicle active-obstacle avoidance path-planning method does, however, have some drawbacks. The standard APF-based self-driving vehicle is unable to obtain information about the state of the world's roads [10]. An extensive body of research has been conducted on APF-based path planning and tracking, with the aim of enhancing obstruction evasion and customizing trajectories for versatile travel demands. Tang et al. [11] ellipticized the distances in the conventional repulsive potential field. To address the local minimum problem, An et al. [12] suggested a novel obstacle-point construction approach. To increase the planning path's smoothness, Xiu Caijing et al. [13] coupled the vehicle restrictions with the objective function. This strategy, however, was only able to address the vehicle path-planning problem in static environments; it ignored the path-planning problem in dynamic environments, making it challenging to use in XEautomatic driving. The approach is straightforward in theory and performs well in real-time. In real applications, however, it is simple to run into issues with local optimal solutions and goal unreachability due to a lack of constraints like vehicle dynamics. The resilience of the algorithm is impacted by the parameters [14].

By deciding on a strategy to enhance the heuristic of the search and increase the applicability of the algorithm, Song et al. [15] improved the smart droplet algorithm [16]. Wang et al. offered a technique to provide advice for corrective speed, reducing the detrimental effects of finite rationality. Jian et al. [17] refined the ant colony algorithm by combining it with the artificial potential field approach for global and local planning. To increase the algorithm's viability, Liu et al. [18] integrated the artificial potential field method with the composite force field to relocate the sampling sites with a tendency for collusion to the region of no collusion. In order to overcome the shortcomings of the APF algorithm, such as its propensity to easily fall into local minima for virtual impediments, Zheng et al. [19] introduced a new minimal criterion and improved the local path-planning method. The local minimization problem was resolved by Matoui [20] and colleagues using a non-minimum speed approach. To solve the local minimization problem brought on by obstructions near the target, Ning et al. [21] suggested a safe distance. A better active filter was then used to design an obstacle-avoidance controller.

Path tracking control is a critical technology for self-driving cars, typically implemented through active steering or differential braking [22]. Various methods have been explored by researchers to address the route tracking problem of self-driving cars, such as proportional integral differential (PID) control, linear self-resistance control [23], pure tracking models, fuzzy adaptive control, and model predictive control [24]. However, the implementation of real-time path tracking faces significant technical challenges under

complex conditions. This is due to differential braking's impact on the vehicle's longitudinal motion, coupled with the inherent complexity and uncertainty in predicting the path of high-speed vehicles. These factors intertwine to create a demanding environment for achieving accurate and responsive path tracking. Active steering encounters notable technical hurdles in complex operational scenarios. Implementing odel predictive control (MPC) methods offers a solution by significantly enhancing control performance. This is achieved through the optimization of the objective function, concurrently factoring in the vehicle's kinematic and dynamic characteristics. By doing so, MPC not only improves control efficacy but also ensures that the vehicle's movement and stability are considered in the control strategy. To construct predictive control for tracking yaw stability, Zhou Li-Hua et al. [25] adopted the linear quadratic regulator (LQR) technique. Wu et al. [26] proposed a new strategy based on MPC and connected vehicles (CVs) for metering and speed guidance control of urban highway entrance ramps. To achieve adaptive optimization of predictive views, Wang et al. [27] suggested an MPC-based route tracking method based on variable predictive views. Morales et al. [28] engineered an omnidirectional system to achieve trajectory tracking, integrating a multilevel control strategy with a Linear Quadratic Regulator (LQR) trajectory tracking controller. This integration was pivotal to minimizing the error associated with trajectory tracking. The fundamental rationale and core objective of path tracking for autonomous vehicles is to drastically diminish the discrepancy between the actual path taken and the intended route throughout the autonomous driving process. This precision is crucial for the safe and efficient navigation of driverless vehicles. Pure tracking control, linear quadratic regulator control, and model predictive control are the current leading route-tracking control approaches. The core contribution of this research is to design a path planner that integrates potential field principle and optimal control strategy to realize the obstacle avoidance function of autonomous vehicles and strictly follow the vehicle's dynamic characteristics. This innovative scheme cleverly combines the advantages of potential field method and optimal path planning, allowing flexibility to incorporate multiple potential factors when seeking the best path to meet obstacles, road layout, and vehicle dynamic characteristics. In contrast, the traditional optimal control path-planning system often only regards obstacles and road edges as limiting conditions or a single cost function [29–33], which fails to fully reflect the differences between various obstacles and road structures. Our approach is unique in that it gives the optimal control problem greater flexibility and pertinence and can be adapted according to the different characteristics of obstacles and roads. Furthermore, we adopt a quadratic model predictive controller to deal with obstacle avoidance challenges in two-dimensional space.

The methodological contributions of this paper are as follows: We refine the standard artificial potential field (APF) method by incorporating a distance adjustment factor, a safe distance protection model, and a virtual sub-target potential field to resolve target unreachability and local minimum issues. A dynamic road repulsive potential field, based on safety distance, optimizes path planning in dynamic environments. The enhanced APF method, with new models and algorithms, boosts autonomous vehicle obstacle-avoidance efficiency, safety, and adaptability to dynamic obstacles, crucial for real-world operations. It improves path planning accuracy, avoids unreachable paths or local optima, and exhibits superior real-time responsiveness and stability. To design optimal paths, the enhanced APF method is applied alongside a vehicle dynamics model, based on the bicycle model principle, linearized and discretized, with a path-tracking model constructed. An optimal predictive control objective function, constrained by variables, minimizes the control command's cost function. Through the co-simulation of MATLAB R2020a/Simulink and CarSim 2019.1, the lower limit of the roll angle required by the optimized vehicle to avoid obstacles in 40, 50, and 60 km /h lane changes is reduced from 11 to 5°. and the upper limit is reduced from 15 to 10°. The maximum fluctuation range of the lateral angle is reduced from 11 to 7°, while the lateral sideslip angle is reduced by 3 to 5°. In addition, the vertical support force of the front and rear wheels increased from 1000 to 1450 N, and the lower limit of the fluctuation starting point of the vertical support force of the front and rear

wheels increased from 950 to 1100 N. The performance of obstacle avoidance and tracking is verified under different dynamic obstacle scenarios as well as different speed parameters.

The article structure is as follows:

1. Section 2 details the collision-avoidance system description and framework, and analyzes autonomous obstacle avoidance and path-planning theory, as well as research based on the optimization of artificial potential field method for autonomous driving vehicles.
2. In Section 3, the vehicle dynamics model is proposed to provide theoretical support for the path tracking controller.
3. In Section 4, the tracking control principle of the DLQR algorithm is analyzed.
4. In Section 5, the path-planning algorithm is experimentally verified. In Section 6, the path-tracking control experiment is analyzed by combining with CarSim–Simulink to change the speed class in different obstacle scenarios.

2. Path Planning for Autonomous Obstacle-Avoidance Based on an Improved APF Algorithm

2.1. Collision-Avoidance System Description and Framework

Traffic accidents due to vehicle collisions are common, and collision avoidance systems aim to prevent such incidents by developing algorithms that avert frontal impacts. The system implements emergency braking through longitudinal and lateral control, with lateral maneuvering being more effective in confined spaces because of its shorter reaction time. With precise calculations and steering adjustments, the automated driving system optimizes lateral control and significantly improves driving safety. Our focus is on technology that instantly senses the environment and makes quick decisions about turning, ensuring stable and comfortable driving with high adaptability to actual road conditions. The object of the collision-avoidance framework is to closely follow the predetermined path, generate a collision-free route, and adapt to changing obstacles. The system consists of virtual environment simulation, path control, and collision-free path generation modules. The potential field method, derived from Khatib's 1985 theory, uses a virtual force field to plan a path. In this model, a gravitational force pulls the vehicle towards the target, while a repulsive force helps the vehicle avoid obstacles. By calculating these gravitational and repulsive forces, the vehicle's movement is controlled to avoid obstacles and travel along a safe path. This method provides rapid feedback, simple mathematical modeling, and closed-loop control, allowing it to produce a smooth, safe path with considerable robustness.

2.2. Road Potential Field Model

For autonomous driving to be safe, accurately modeling a secure road boundary potential field function is crucial. It is assumed that the route used by the primary vehicle has two lanes, as illustrated in Figure 1. On the left and right sides of the road are designated lanes A and B, respectively, with lane B serving as the primary travel lane and lane A as the overtaking lane. The road coordinate system's horizontal and vertical coordinates are x and y, respectively. In order to avoid a collision and keep the vehicle safe, the main vehicle should overtake any obstacle vehicles on the road, as shown in Figure 1, in accordance with the design principle of the active obstacle avoidance system for self-driving vehicles. In order to prevent more serious traffic collisions, the primary vehicle should also avoid approaching or crossing the road boundary on either side, keeping within the safe limits of the designated lanes.
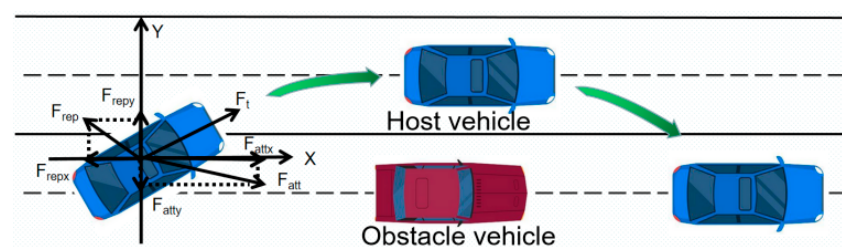

Figure 1. Principle of autonomous collision avoidance.

2.2.1. Hazardous Potential Fields at Road Boundaries

The roadway lateral hazard potential field as a function of Px with x-direction is expressed as [34]:

$$Px = \exp[-(4-|X-2|)^2] \tag{1}$$

The longitudinal hazard potential field of the road as a function of the x-direction Pz is expressed as:

$$Pz = \frac{\exp[-(X-2)^2]}{2} \tag{2}$$

The longitudinal hazard potential field of the road as a function of the y-direction Py is expressed as:

$$P_y = \begin{cases} 0, & |Y-Y_0| \leq D_b \\ \frac{|Y-Y_0|-D_b}{D_t-D_b}, & D_b \leq |Y-Y_0| \leq D_t \\ 1, & |Y-Y_0| \geq D_t \end{cases} \tag{3}$$

where (X_0, Y_0) are the obstacle coordinates, D_b is the main vehicle safety distance and D_t is the transition region. The function U_r of the road hazard potential field is expressed as:

$$U_r = P_x + P_y P_z \tag{4}$$

The expression for the lateral repulsion of the road is:

$$Frx = \begin{cases} 2sign(X-2)(|X-2|-4)\exp[-(|X-2|-4)^2], & |Y-Y_0| \leq D_b \\ \left(\dfrac{4\exp[-(|X-2|-4)^2]sign(X-2)(|X-2|-4)(D_t-D_b)}{2(D_t-D_b)} \right. & \\ \left. +\dfrac{\exp[-(X-2)^2](|Y-Y_0|-D_b)(2X-4)}{2(D_t-D_b)}\right), & D_b \leq |Y-Y_0| \leq D_t \\ (2sign(X-2)(|X-2|-4)\exp[-(|X-2|-4)^2] & \\ +\exp[-(X-2)^2](X-2)), & |Y-Y_0| \geq D_t \end{cases} \tag{5}$$

The expression for the longitudinal repulsive force on the pavement is:

$$F_{ry} = \begin{cases} \frac{-sign(Y-Y_0)\exp[-(X-2)^2]}{2(D_t-D_b)}, & D_b \leq |Y-Y_0| \leq D_t \\ 0, & else \end{cases} \tag{6}$$

The attraction potential field expression U_{att} is:

$$U_{att} = \frac{|X-X_r| + |Y-Y_v-\frac{1}{2}D_s|}{100} \tag{7}$$

where D_s denotes the distance range of the vehicle's forward path search and X_r denotes the center line of the overtaking lane. Y_v is the longitudinal position of the center of mass of the main vehicle in the coordinate system.

The roadway lateral gravitational force expression F_{xatt} is:

$$F_{xatt} = \frac{-sign(X-X_r)}{100} \tag{8}$$

The roadway longitudinal attraction expression F_{yatt} is:

$$F_{yatt} = \frac{-sign(Y-Y_0-\frac{1}{2}D_s)}{15} \tag{9}$$

2.2.2. Safe Distance Protection Model

Vehicle braking, steering, and road structural parameters need to be taken into account when building the obstacle vehicle potential field. Additionally, it is crucial to guarantee that the primary vehicle has enough time to make decisions regarding steering behavior and high stability when performing active obstacle avoidance maneuvers.

For active obstacle avoidance, it is therefore important to make sure that the safety distance D_b and transition distance D_t are at least [35]:

$$D_b = \frac{M(v_1{}^2 - v_2{}^2)}{8F_m} + \frac{L_1}{2} \tag{10}$$

$$D_t = D_b + 10 \tag{11}$$

where v_1 and v_2 are the initial speeds of the main vehicle and the obstacle vehicle on the road, respectively, F_m is the maximum braking force of one wheel, M is the total mass of the main vehicle, and L_1 is the length of the body of the obstacle vehicle.

2.3. Classical Artificial Potential Field Method

2.3.1. Target Point Gravitational Field

Figure 2a shows the traditional artificial potential field method's gravitational field function:

$$U_{att} = \frac{1}{2}K_{att}(X - X_g)^2 \tag{12}$$

where X represents the autonomous vehicle's position, U_{att} stands for the gravitational potential at the goal point, K_{att} denotes the positive real scalar describing the field's gain, and X_g indicates the aimed-at position of the autonomous car. Herein lies the determination of the gravitational potential field's negative gradient:
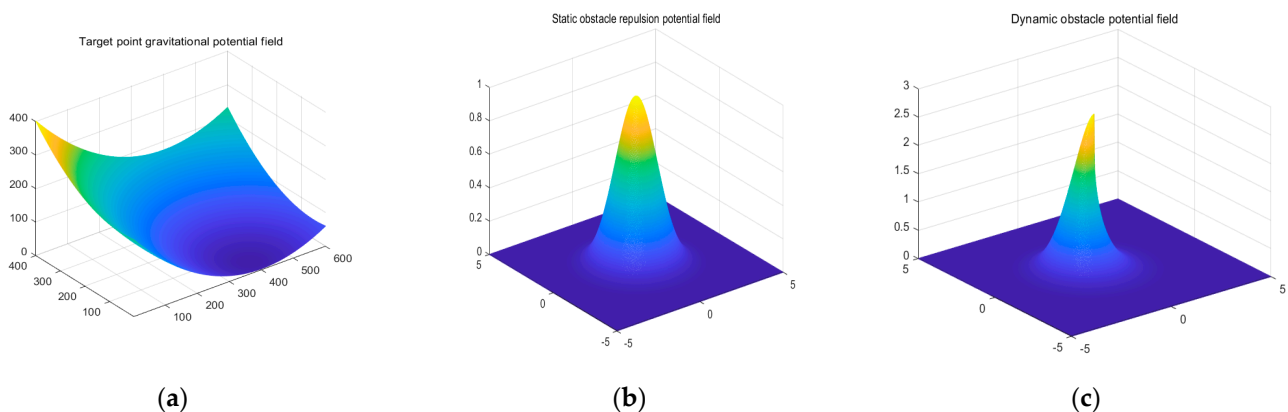
$$F_{att} = -grad(U_{att}) = k(X_g - X) \tag{13}$$

| (a) | (b) | (c) |

Figure 2. APF three-dimensional potential field. Figure (**a**) shows the attractive potential field of the target point. Figure (**b**) shows the repulsive potential field of the static obstacle. Figure (**c**) shows the repulsive potential field of the dynamic obstacle.

2.3.2. Obstacle Vehicle Repulsion Field

According to Figure 2b, static obstacle repulsive potential field and Figure 2c, dynamic obstacle repulsive potential field, the specific potential field function of the natural potential field of repulsive force can be expressed as follows [36]:

$$U_{rep} = \begin{cases} \frac{1}{2}k_{rep}\left(\frac{1}{D} - \frac{1}{D_0}\right)^2 & D \leq D_0 \\ 0, & D > D_0 \end{cases} \tag{14}$$

where U_{rep} is the obstacle vehicle repulsive force field; k_{rep} is the repulsive potential field gain coefficient, a positive real number; D is the straight line between the car and the obstacle vehicle (shortest distance); D_0 is the obstacle vehicle repulsive force that can affect the maximum range.

$$F_{rep} = \begin{cases} k_{rep}(\frac{1}{D} - \frac{1}{D_0})\frac{1}{D^2}\frac{\delta D}{\delta X}, & D \leq D_0 \\ 0, & D > D_0 \end{cases} \tag{15}$$

2.4. Optimization of the Artificial Potential Field Method

2.4.1. Boosted Repulsive Field Function: Distance Adjustment Enhanced

An advanced repulsive potential field function is devised from the baseline model, characterized by an increased distance adjustment parameter to diminish repulsive forces near the destination. This innovation counteracts the inherent limitation preventing target acquisition in classic artificial potential field methodologies. Following is the presentation of this optimized function:

$$U_{rep} = \begin{cases} \frac{1}{2}k_{rep}(\frac{1}{D} - \frac{1}{D_0})^2[1 - \exp\frac{(X - X_g)^2 + (Y - Y_g)^2}{R^2}], & D \leq D_0 \\ 0, & D > D_0 \end{cases} \tag{16}$$

where $[X, Y]$ are the autonomous vehicle's real-time coordinate points; $[X_g, Y_g]$ are the coordinates of the target point; and R is the radius of the autonomous vehicle.

The repelling force of the obstacle vehicle's potential field can be determined by:

$$-U'_{rep}(x) = -k_{rep}(X - X_g)(\frac{1}{D} - \frac{1}{D_0})^2 \exp[\frac{(X - X_g)^2 + (Y - Y_g)^2}{R^2}] + k_{rep}(\frac{1}{D} - \frac{1}{D_0})[1 - \exp(\frac{(X - X_g)^2 + (Y - Y_g)^2}{R^2})]\frac{X - X_0}{D^3} \tag{17}$$

$$-U'_{rep}(Y) = -k_{rep}(Y - Y_g)(\frac{1}{D} - \frac{1}{D_0})^2 + k_{rep}(\frac{1}{D} - \frac{1}{D_0})[1 - \exp(\frac{(X - X_g)^2 + (Y - Y_g)^2}{R^2})]\frac{Y - Y_0}{D^3} \tag{18}$$

$$\left|F_{rep}\right| = \sqrt{U'_{rep}(X)^2 + U'_{rep}(Y)^2} \tag{19}$$

From Equations (3) and (16), adjustments to the repulsive potential occur exclusively close to the destination, yet the improved approach can hinder the search algorithm's efficiency [37]. Therefore, in this paper, the repulsive force is improved, i.e., the distance adjustment factor is added to the original repulsive force. The repulsive force formula is:

$$|F_{rep}| = \begin{cases} \frac{k_{rep}}{D^2}(\frac{1}{D} - \frac{1}{D_0})[1 - \exp(\frac{(X - X_g)^2 + (Y - Y_g)^2}{R^2})], & D \leq D_0 \\ 0, & D > D_0 \end{cases} \tag{20}$$

Through Equation (16), the repulsive potential field gains strength; consequently, the vehicle's repulsive force decays toward nil at the destination, factoring in the car's radius to elevate both route dependability and security. The improved potential field function addresses the target unreachability issue commonly found in traditional potential field methods, while also mitigating extreme values of the repulsive force and preventing scenarios with excessive repulsion.

2.4.2. Sub-Target Virtual Point Intervention

After confirming that the primary vehicle is trapped in a local minimum, the decision of the virtual target point's position must be taken into account. First, care must be taken to prevent the inclusion of this point from causing it to mix with the gravitational or repulsive force and imprison the primary vehicle once more in the local minima. Second, in accordance with the design principles of the active obstacle avoidance system, the primary vehicle should attempt to maintain the center line of the lane during actual driving. In other words, the main vehicle should preferentially reach the center of the neighboring lane when engaging obstacle avoidance behavior. As a result, lane B's centerline should be set at point P1's horizontal coordinate X1. When the main vehicle enters a localized

minimal point, point P1 should also guarantee that it can be subjected to a significant attractive potential energy. Figure 3 shows that the primary vehicle can then successfully execute active obstacle avoidance and quickly escape the local minima. In conclusion, the virtual target point's coordinates are set as $P_1(X_1, \frac{Y_0 + Y_v}{2})$, and then, using the spatial geometric relationship, the minimum distance between the virtual target point P1 and the main vehicle's center of mass is calculated as:

$$d_{\min} = \sqrt{(X_v - X_1)^2 + (Y_v - \frac{Y_0 + Y_v}{2})^2} \tag{21}$$
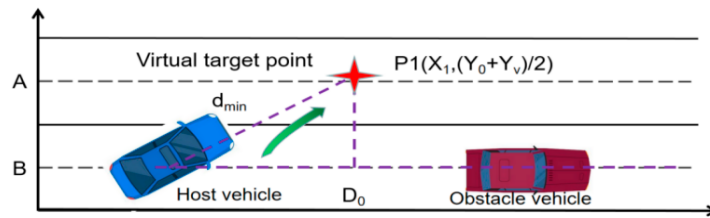
Figure 3. Sub-target virtual potential field.

2.4.3. Sub-Target Virtual Potential Field Attraction Function

To ensure that the newly introduced virtual target point may successfully address the local minima problem, we provide an appropriate attractive potential field function. This feature must be able to rapidly activate and operate as the main influencing factor in the event that the main vehicle is trapped in the local minima. The gravitational potential field function of the sub-target is as follows:

$$U_{vir} = \frac{1}{2} K_{vir} d_{\min}^2 \tag{22}$$

where K_{vir} is the field gain coefficient for the attraction potential.

The gravitational potential field's negative gradient F_{vir} is the associated potential field force. In order to express the second virtual target gravitational potential field force F bundle, the following functions are used:

$$F_{vir} = -\nabla U_{vir} = -K_{vir} d_{\min} \tag{23}$$

The host vehicle was pointed in the direction of the second virtual potential field force. Once the issue of becoming trapped at the minimum point is resolved and the obstacle vehicle is successfully avoided, the virtual target point is then deactivated. Environmental elements such as road margins, fixed obstructions, and moving obstructions will be considered in this effort by creating relevant potential functions. The exclusion potential function is used to determine the collision risk in order to prevent a collision between the self-driving vehicle and road edges and objects.

The self-driving vehicle is traveling on a straight, two-lane road, and the total potential field of the potential function consists of the potential field values of the road edges, obstacles, and target points. Figure 4 presents a 2D contour plot of the generic potential showing the collision-free trajectory of the vehicle's path planning.

The total potential field function can be expressed as:

$$U_{total} = \sum_{i=1}^{n} U_{ri} + U_{\text{rep}} + U_{att} \tag{24}$$

When the self-driving vehicle is caught in the local minima environment during driving, the sub-target virtual potential field triggers and intervenes in the controller

system to help the self-driving vehicle escape from the local optimum, at which time the potential function can be expressed as:

$$F_{\text{total}} = \sum_{i=1}^{n} F_{\text{ri}} + F_{\text{rep}} + F_{\text{att}} \tag{25}$$

When the self-driving vehicle is caught in the local minima environment during driving, the sub-target virtual potential field triggers and intervenes in the controller system to help the self-driving vehicle escape from the local optimum, at which time the potential function can be expressed as:

$$U_{total} = \sum_{i=1}^{n} U_{ri} + U_{\text{rep}} + U_{att} + U_{\text{vir}} \tag{26}$$

The potential field is rationally represented as:

$$F_{\text{total}} = \sum_{i=1}^{n} F_{\text{ri}} + F_{\text{rep}} + F_{\text{att}} + F_{vir} \tag{27}$$
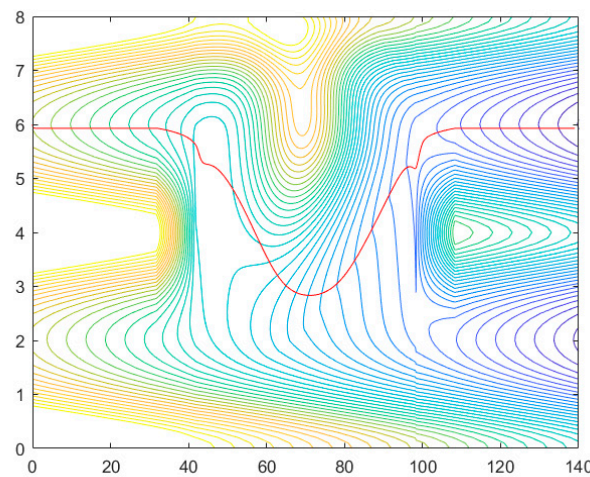
Figure 4. Contour maps of potential fields and collision-free trajectories.

3. Vehicle Dynamics Modeling

3.1. Conditional Assumptions

Vehicle dynamics modeling's fundamental premise is to investigate the relationship between each object's relative motion and mechanical properties in order to give accurate control of the vehicle during path tracking. The actual modeling technique makes the following assumptions in order to streamline the algorithm's solution procedure and improve path tracking efficiency:

1. Exceptional road quality enables the vehicle to execute motion confined to a plane, parallel to the road surface, in pure two-dimensional dynamics;
2. Given the rigidity of the vehicle, considerations for suspension system impacts are omitted;
3. The left and right wheel angles do not alter when the vehicle rotates with the front wheels;
4. How the vehicle tires are coupled longitudinally and laterally is not taken into account;
5. The impact of aerodynamics is disregarded;
6. The transfer of the vehicle load is disregarded;
7. In order to streamline the study, the bicycle model is created while taking into account the characteristics of the reference path, as illustrated in Figure 5.
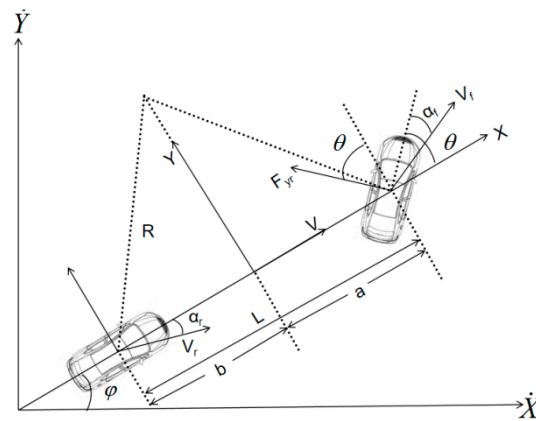
Figure 5. Principles of vehicle dynamics.

3.2. Vehicle Kinematics Modeling

Vehicle kinematics modeling can be expressed as Equations (28)–(31):

$$\dot{X} = v \cos \varphi \tag{28}$$

$$\dot{Y} = v \sin \varphi \tag{29}$$

since the formula:

$$\begin{aligned} \dot{\varphi} &= \frac{v}{R} \\ \tan \theta &= \frac{L}{R} \end{aligned} \tag{30}$$

So there is:

$$\dot{\varphi} = \frac{v \tan \theta}{L} \tag{31}$$

where θ is the front wheel angle, L is the vehicle wheelbase, and R is the turning radius.

3.3. Simplified Model of Vehicle Dynamics

Despite its tracking accuracy at low speeds in smooth conditions, the vehicle's kinematics model can be challenging to use to execute path tracking when the vehicle's speed increases and the path curvature varies. The nonlinear vehicle dynamics model calculation is too difficult. The tiny angle assumption, which turns each angle in the model into an ideal condition, is presented to lessen the burden of data processing. In this case, a vehicle dynamics model that considers the vehicle's tire characteristics and dynamic effects must be developed in order to accurately track the reference path. It is assumed that the vehicle's front wheel rotates at a small angle and that the longitudinal velocity is constant. The small-angle hypothesis approximates as follows:

$$\sin \theta \approx 0 \tag{32}$$

$$\cos \theta \approx 1 \tag{33}$$

$$\tan \theta \approx 0 \tag{34}$$

By invoking Newton's principles of force, we derive the dynamic expressions governing the vehicle's behavior:

$$ma_y = F_{yf} \cos \theta + F_{yr} \tag{35}$$

The moment equation is:

$$F_{yf} \cos \theta \cdot \mathrm{a} - F_{yr} \cdot b = I \ddot{\varphi} \tag{36}$$

where a and b are the distance from the front and rear tires to the center of gravity of the vehicle, respectively.

The relationship between a_y and y is:

$$v_y = \dot{y}$$
$$a_y = \ddot{y} + v_x \dot{\varphi} \tag{37}$$

$$F_f = C_{\alpha f} \cdot \alpha_f$$
$$F_r = C_{\alpha r} \cdot \alpha_r \tag{38}$$

where $C_{\alpha f}$ and $C_{\alpha r}$ are the lateral deflection stiffness of the front and rear tires, respectively. The lateral deflection stiffness is expected to be negative, with the theoretical knowledge of the car and vehicle dynamics related to knowledge of coordinate systems in line with the cognitive logic of physics.

The front and rear wheel side deflections are calculated as:

$$\alpha_{\alpha f} = \frac{\dot{\varphi} \cdot a + v_y}{v_x} - \theta$$
$$\alpha_{\alpha r} = \frac{v_y - \dot{\varphi} \cdot b}{v_x} \tag{39}$$

The front and rear side deflection forces are:

$$F_f = C_{\alpha f} \cdot \left(\frac{\dot{\varphi} \cdot a + v_y}{v_x} - \theta \right)$$
$$F_r = C_{\alpha r} \cdot \left(\frac{v_y - \dot{\varphi} \cdot b}{v_x} \right) \tag{40}$$

By substituting (31) and (34) into Equation (29), we obtain:

$$m(\dot{v}_y + v_x \cdot \dot{\varphi}) = C_{\alpha f}\left(\frac{\dot{\varphi} \cdot a + v_y}{v_x} - \theta \right) + C_{\alpha r}\left(\frac{v_y - \dot{\varphi} \cdot b}{v_x} \right) \tag{41}$$

By substituting (34) into Equation (30), we obtain:

$$I\ddot{\varphi} = a \cdot C_{\alpha f}\left(\frac{\dot{\varphi} \cdot a + v_y}{v_x} - \theta \right) - b \cdot C_{\alpha r}\left(\frac{v_y - \dot{\varphi} \cdot b}{v_x} \right) \tag{42}$$

From $v_y = y$, substituting into Equations (6), (7), (15), and (16) accordingly outline the vehicle's lateral state space model, defining it comprehensively:

$$\begin{pmatrix} \ddot{y} \\ \ddot{\varphi} \end{pmatrix} = \begin{pmatrix} \frac{C_{\alpha f} + C_{\alpha r}}{m v_x} & \frac{a \cdot C_{\alpha f} - b \cdot C_{\alpha r}}{m v_x} - v_x \\ \frac{a \cdot C_{\alpha f} - b \cdot C_{\alpha r}}{I v_x} & \frac{a^2 \cdot C_{\alpha f} + b^2 \cdot C_{\alpha r}}{I v_x} \end{pmatrix} \cdot \begin{pmatrix} \dot{y} \\ \dot{\varphi} \end{pmatrix} + \begin{pmatrix} -\frac{C_{\alpha f}}{m} \\ -\frac{C_{\alpha f}}{I} \end{pmatrix} \cdot \theta \tag{43}$$

4. Path Tracking for Autonomous Vehicles Based on DLQR Control Algorithm

4.1. Path Tracking Control Architecture

Despite the vehicle kinematics model's high tracking accuracy at low speeds in smooth conditions, the dynamics model of an autonomous vehicle reveals that both feed-forward control and feedback are essential to handle high-speed or complex driving scenarios. To generate the proper steering angle for the self-driving car, the DLQR control approach is employed. In an autonomous driving system, combining feed-forward control with DLQR (Discrete Linear Quadratic Optimal Regulator) control can give full play to the advantages of both. Feed-forward control can be used to predict and compensate for deviations due to external interference or system uncertainty, while DLQR control can be used to optimize vehicle trajectory and speed. In practical applications, feed-forward control is often designed as an additional control that is added to the output of the DLQR controller. In this way, the DLQR controller is responsible for providing the basic control signal, while the feed-forward controller is responsible for providing additional control signals that compensate for the predicted deviation for optimal driving performance. In order to lessen the disturbances caused by path curvature, the controller makes use of the

reference path's preview information. Conversely, the LQR algorithm exhibits a superior adaptability to fluctuations in longitudinal speed during course adherence. Its design is geared towards mitigating the real-time lateral deviation and directional discrepancies precipitated by external perturbations, thereby ensuring a more robust and responsive control mechanism. Figure 6 depicts the control model framework.
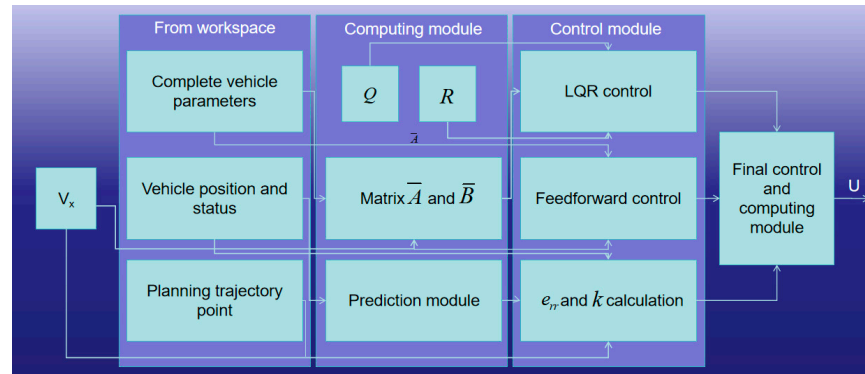

Figure 6. Framework of DLQR tracking control algorithm.

4.2. Calculation of Error Parameters

The closest planning point to the true motion point is found by traversing the planning path points such that the sequence of points is denoted as $D_{\min}$.

$$\begin{pmatrix} x_r \\ y_r \\ \theta_r \\ k_r \end{pmatrix} = \begin{pmatrix} x_1 & x_2 & \cdots & x_n \\ y_1 & y_2 & \cdots & y_n \\ \theta_1 & \theta_2 & \cdots & \theta_n \\ k_1 & k_2 & \cdots & k_n \end{pmatrix} \tag{44}$$

Then the tangential unit vector and the normal unit vector are:

$$\vec{\tau} = \begin{pmatrix} \cos(\theta_{D\min}) \\ \sin(\theta_{D\min}) \end{pmatrix}, \vec{\eta} = \begin{pmatrix} -\sin(\theta_{D\min}) \\ \cos(\theta_{D\min}) \end{pmatrix} \tag{45}$$

The distance error is:

$$d_{err} = \begin{pmatrix} x - x_{D\min} \\ y - y_{D\min} \end{pmatrix} \tag{46}$$

where (x, y) is the true motion point and $(x_{D\min}, y_{D\min})$ is the traversal matching point-normal distance error and tangential distance error, respectively:

$$e_d = \vec{\eta}^T \cdot d_{err}, e_s =^T \vec{\tau}^T \cdot d_{err} \tag{47}$$

The angle between the velocity of the planned path point and the *x*-axis is:

$$\theta_r = \theta_{\min} + k_{D\min} \cdot e_s \tag{48}$$

The normal distance error rate is:

$$\dot{e}_d = v_y \cos(\varphi - \theta_r) + v_x \sin(\varphi - \theta_r) \tag{49}$$

The vehicle's transverse angle error is:

$$e_\varphi = \varphi - \theta_r \tag{50}$$

The vehicle's transverse swing angular velocity error is:

$$\dot{S} = \frac{v_x \cos(\varphi - \theta_r) - v_y \sin(\varphi - \theta_r)}{1 - k_{D\min} e_d}$$
$$\dot{e}_\varphi = \dot{\varphi} - k_{D\min} \cdot \dot{S} \tag{51}$$

The curvature of the planning path points is:

$$k_r = k_{D\min} \tag{52}$$

In summary, the error vector of the lateral error differential equation can be obtained as:

$$e_{rr} = [e_d, \dot{e}_d, e_\varphi, \dot{e}_\varphi] \tag{53}$$

The component of the velocity in the y-direction and the acceleration are:

$$v_y = \dot{e}_d - v_x e_\varphi$$
$$\dot{v}_y = \ddot{e}_d - v_x \dot{e}_\varphi \tag{54}$$

The vehicle's transverse swing angular velocity and acceleration are:

$$\dot{\varphi} = \dot{e}_\varphi + \dot{\theta}_r$$
$$\ddot{\varphi} = \ddot{e}_\varphi \tag{55}$$

Substituting the above Equations (45)–(53) into the differential equation for the two-degree-of-freedom dynamics, the differential equation for the transverse error is obtained as:

$$v_y = \left(\frac{C_{\alpha f} + C_{\alpha r}}{m v_x}\right)\dot{e}_d + \left(-\frac{C_{\alpha f} + C_{\alpha r}}{m}\right)e_\varphi + \left(\frac{a C_{\alpha f} - b C_{\alpha r}}{m v_x}\right)\dot{e}_\varphi + \left(\frac{a C_{\alpha f} - b C_{\alpha r}}{m v_x} - v_x\right)\dot{\theta}_r + \left(-\frac{C_{\alpha f}}{m}\right)\delta_f \tag{56}$$

$$\ddot{e}_\varphi \approx \ddot{\varphi} = \left(\frac{a C_{\alpha f} - b C_{\alpha r}}{I v_x}\right)\dot{e}_d + \left(-\frac{a C_{\alpha f} - b C_{\alpha r}}{I}\right)e_\varphi + \left(\frac{a^2 C_{\alpha f} + b^2 C_{\alpha r}}{I v_x}\right)\dot{e}_\varphi + \left(\frac{a^2 C_{\alpha f} + b^2 C_{\alpha r}}{I v_x}\right)\dot{\theta}_r + \left(-\frac{a C_{\alpha f}}{I}\right)\delta_f \tag{57}$$

Written in matrix form, this becomes:

$$\begin{pmatrix} \dot{e}_d \\ \ddot{e}_d \\ \dot{e}_\varphi \\ \ddot{e}_\varphi \end{pmatrix} = \begin{pmatrix} 0 & 1 & 0 & 0 \\ 0 & \frac{C_{\alpha f} + C_{\alpha r}}{m v_x} & -\frac{C_{\alpha f} + C_{\alpha r}}{m} & \frac{a C_{\alpha f} - b C_{\alpha r}}{m v_x} \\ 0 & 0 & 0 & 1 \\ 0 & \frac{a C_{\alpha f} - b C_{\alpha r}}{I v_x} & -\frac{a C_{\alpha f} - b C_{\alpha r}}{I} & \frac{a^2 C_{\alpha f} + b^2 C_{\alpha r}}{I v_x} \end{pmatrix} \begin{pmatrix} e_d \\ \dot{e}_d \\ e_\varphi \\ \dot{e}_\varphi \end{pmatrix} + \begin{pmatrix} 0 \\ -\frac{C_{\alpha f}}{m} \\ 0 \\ -\frac{a C_{\alpha f}}{I} \end{pmatrix} \delta_f + \begin{pmatrix} 0 \\ \left(\frac{a C_{\alpha f} - b C_{\alpha r}}{m v_x} - v_x\right) \\ 0 \\ \left(\frac{a^2 C_{\alpha f} + b^2 C_{\alpha r}}{I v_x}\right) \end{pmatrix} \dot{\theta}_r \tag{58}$$

4.3. Feed-Forward Control

Aiming squarely at accuracy, the refined optimal feed-forward controller targets elimination of lateral discrepancies induced by curved paths. In order to achieve this goal, the algorithm cleverly introduces the preview information of path curvature, which is key data that can be accurately obtained directly from the pre-planned path, so as to ensure the efficiency and accuracy of the controller when dealing with complex paths. The feed-forward control can be defined as δ_{fa}, expressed as Equations (59) and (60).

$$\delta_{fa} = \frac{\dot{\theta}_r}{v_x}\left[a + b - b \cdot k_3 - \frac{m \cdot v_x}{a + b}\left(\frac{b}{C_f} + \frac{a}{C_r}k_3 - \frac{a}{C_r}\right)\right] \tag{59}$$

$$\dot{S} = \frac{v_x \cos e_\theta - v_y \sin e_\theta}{1 - K e_d} \tag{60}$$

The defining equation for the curvature *K* is:

$$K = \frac{\ddot{y}}{(1+\dot{y})^{\frac{3}{2}}} = \frac{\dot{\theta}}{\dot{S}}$$ (61)

It is obtained from the defining equation of *K*:

$$\dot{\theta}_r = K\dot{S}$$ (62)

Since the expression is too complex, it is approximated here as $|K| \ll 1$, $|e_\theta| \ll 1$, $|V_y| \ll 1$ in a drift-free state.

$$\dot{\theta}_r = K \cdot \dot{S} \approx K \cdot v_x$$ (63)

Thus, substituting the above Equation (61) into Equation (57), we obtain:

$$\delta_{fa} = K[a + b - b \cdot k_3 - \frac{m \cdot v_x}{a+b}(\frac{b}{C_f} + \frac{a}{C_r}k_3 - \frac{a}{C_r})]$$ (64)

where δ_{fa} is feed-forward control Angle input, k_3 is the third element of the K-matrix calculated by the feedback control module, v_x is the constant longitudinal velocity, m is the mass, and *a*, *b* are the distances from the hub centers of the vehicle's front and rear wheels to the center of mass, respectively. The vehicle's front and back wheels' lateral deflection stiffnesses are represented by the values C_f and C_r, respectively.

The feed-forward control input is *f*. External perturbations hinder the controller's ability to sustain negligible lateral deviation. In order to reduce the lateral error, it is important to develop an external disturbance feedback controller.

4.4. Forecasting System

Because the vehicle motion comes with inertia effects, the steering control has a lag, so it is necessary to add a prediction module to improve the vehicle motion lag to improve the vehicle predictive performance.

The vehicle prediction position point is:

$$x_{pre} = x + v_x t_s \cos\varphi - v_y t_s \sin\varphi$$ (65)

$$y_{pre} = y + v_y t_s \cos\varphi + v_y t_s \cos\varphi + v_x t_s \sin\varphi$$ (66)

The vehicle is predicted to have a transverse swing angle of:

$$\varphi_{pre} = \varphi + \dot{\varphi}t_s$$ (67)

Vehicles are predicted to have a speed of:

$$v_{xpre} = v_x, v_{ypre} = v_y, \dot{\varphi}_{pre} = \dot{\varphi}$$ (68)

4.5. Optimal DLQR Control

Tasked with aligning paths by compensating for lateral errors induced by disruptions, the DLQR controller operates under an assumption of steady forward speed. The vehicle's state-space error dynamics are modeled as:

$$\dot{e}_{rr} = A \cdot e_{rr} + B \cdot u$$ (69)

where $e_{rr} = [e_d, \dot{e}_d, e_\varphi, \dot{e}_\varphi]$, *u* is the feedback steering control command. With the LQR controller utilizing discrete digital inputs and a 0.01-s sampling period, the state space representation requires discretization using Euler's technique.

Hence, expressing the DLQR's discrete model for lateral error dynamics yields:

$$e_{rr}(k+1) = \overline{A} \cdot e_{rr}(k) + \overline{B} \cdot u(k) \tag{70}$$

The optimal steering control command may be expressed as:

$$u(k) = -K \cdot e_{rr}(k) \tag{71}$$

where K is the optimal control gain and K is expressed as Equation (32):

$$K = (R + \overline{B}^T P \overline{B})^{-1} \overline{B}^T P \overline{A} \tag{72}$$

Minimizing the constrained control command's objective cost function via Equation (71), and ascertaining matrix P through the algebraic Riccati equation, Equation (72).

$$J = \sum_{k=0}^{+\infty} (x_k^T Q x_k + u_k^T R u_k) \tag{73}$$

$$P = Q + \overline{A}^T P \overline{A} - \overline{A}^T P \overline{B}(R + \overline{B}^T P \overline{B})^{-1} \overline{B}^T P \overline{A} \tag{74}$$

$$Q = \begin{pmatrix} q_1 & 0 & 0 & 0 \\ 0 & q_2 & 0 & 0 \\ 0 & 0 & q_3 & 0 \\ 0 & 0 & 0 & q_4 \end{pmatrix} \tag{75}$$

The elements on the diagonal matrix correspond to the weights of different state and control quantities: the larger the weights, the more importance we attach to the quantity, i.e., we hope that the quantity will maintain a smaller value during the change process, in other words, the larger the "penalty" for the quantity. Q is the diagonal state cost matrix, which features optimization minimization performance; R = [15] is the input cost matrix, which represents the control realization minimization. Steering parameters, under this methodology, are set as follows: q1 = 25, q2 = 3, q3 = 10, q4 = 4.

From the transverse error differential equation, the matrix $\overline{A}$, $\overline{B}$ is:

$$\overline{A} = \begin{pmatrix} 0 & 1 & 0 & 0 \\ 0 & \frac{C_{\alpha f} + C_{\alpha r}}{m v_x} & -\frac{C_{\alpha f} + C_{\alpha r}}{m} & \frac{a C_{\alpha f} - b C_{\alpha r}}{m v_x} \\ 0 & 0 & 0 & 1 \\ 0 & \frac{a C_{\alpha f} - b C_{\alpha r}}{I v_x} & -\frac{a C_{\alpha f} - b C_{\alpha r}}{I} & \frac{a^2 C_{\alpha f} + b^2 C_{\alpha r}}{I v_x} \end{pmatrix}, \overline{B} = \begin{pmatrix} 0 \\ -\frac{C_{\alpha f}}{m} \\ 0 \\ -\frac{C_{\alpha f}}{I} \end{pmatrix} \tag{76}$$

Matrices $\overline{A}$ and $\overline{B}$ are only related to v_x, $dlqr = (\overline{A}, \overline{B}, Q, R)$, the larger Q is, the better the accuracy, but poor stability is a factor. The larger R is, the smoother the motion process is, the better the comfort and safety, but the tracking effect is poor, so the values of Q and R should be weighed. Finally, the steering angle input is as follow:

$$\delta_f = \delta_{fa} + u_k \tag{77}$$

5. Simulation Verification of Optimized APF-Based Autonomous Vehicle Path Planning for Obstacle Avoidance

5.1. Experimental Parameter Presetting

This study simulates the path planning of autonomous vehicles both before and after the artificial potential field method has been improved. The test road is first chosen as a two-lane road. Each lane will be 3.5 m wide, with a total length of 100 m. The self-driving car's starting point is (0, 2), and its destination position is (100, 2). Additionally,

two dynamic obstacle vehicles with initial positions of (45, 1.75), (60, −1.75), and matching speeds of 15 and 20 km/h are set up for simulation testing.

5.2. Simulation Experiment Analysis

When the obstacle vehicle is moving faster than the rear main vehicle, which is assumed to be moving normally in the traffic lane traveling at 60 km per hour, the space between the two vehicles narrows until it is less than the predetermined safety distance. A reasonable gravitational potential field of the sub-target virtual point is generated by adding the sub-target virtual point, which provides a sub-target virtual point of attraction for the main vehicle that falls into the local minima and local oscillations, allowing it to escape from the issue of local minima and local oscillations. As a result, the preset vehicle safety and transition distance cannot completely eliminate the risk of falling into the local minima. The simulation results are as follows: In Figure 7a–c, the autonomous vehicle initiates its journey from the starting point at a steady pace, deftly navigating past the moving obstacle, vehicle 1, under the guidance of the composite potential field, thereby successfully executing an obstacle-avoidance maneuver with elegance and precision. And while the dynamic obstacle vehicle 2 drives, it progressively changes course to prepare for the subsequent lane change. Due to the influence of the composite potential field (as shown in Figure 7c–e), the autonomous vehicle changes lanes earlier, overtakes from the same lane, successfully avoids the dynamic impediment vehicle 2, and travels smoothly to the target position.
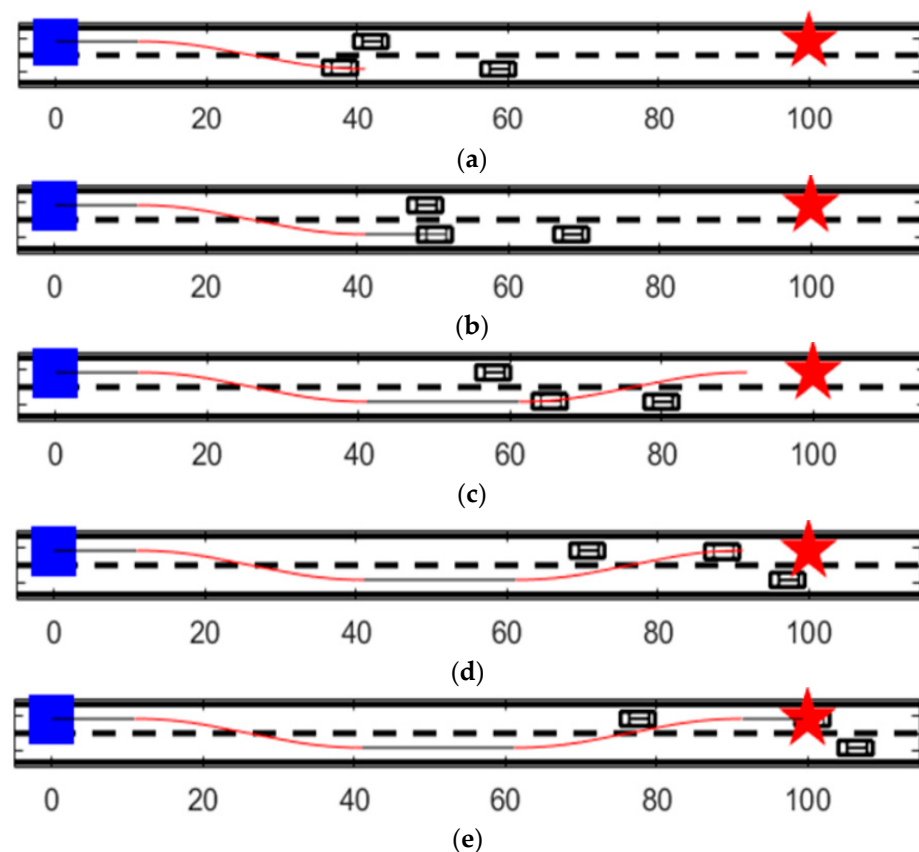

Figure 7. Optimizing APF for overtaking and collision avoidance. (**a**) Changing lanes with combined force; (**b**) changing lanes to overtake; (**c**) lane change and passing complete; (**d**) return to main lane; (**e**) drive smoothly to the target point.

5.3. Conclusion of the Simulation Experiment

The simulation findings accurately represent the precision of the algorithm and show that self-driving cars are capable of avoiding hazards, changing lanes, and overtaking

in dynamic conditions. The enhanced artificial potential field approach increases the speed and degree of path smoothing while also improving the accuracy of the planned paths to suit the actual situation's stability requirements. The increased artificial potential field method used in this work can therefore yield computations with more accuracy and applicability.

6. Joint CarSim and Simulink for Path Tracking Experiment Simulation

6.1. Joint Simulation Platform

The utilization of co-simulation platforms in the realm of autonomous driving has emerged as a prevalent approach. In this study, leveraging a multi-software co-simulation environment, we have developed an enhanced DLQR path-tracking controller grounded in vehicle dynamics. This controller enables the autonomous vehicle to adeptly follow its intended path in both medium- and high-speed traffic scenarios. To evaluate the obstacle avoidance capabilities and safety stability of this optimized DLQR controller, we have employed the reference path derived from an advanced artificial potential field method. This method was used to rigorously test the controller's performance across a spectrum of obstacle configurations and varying speed parameters, ensuring its robustness and reliability in real-world conditions.

6.2. Tracking Control Algorithm Architecture

The self-driving car's body specifications and characteristics are first built up in CarSim. Figure 8 and Table 1 display the characteristics and body measurements.
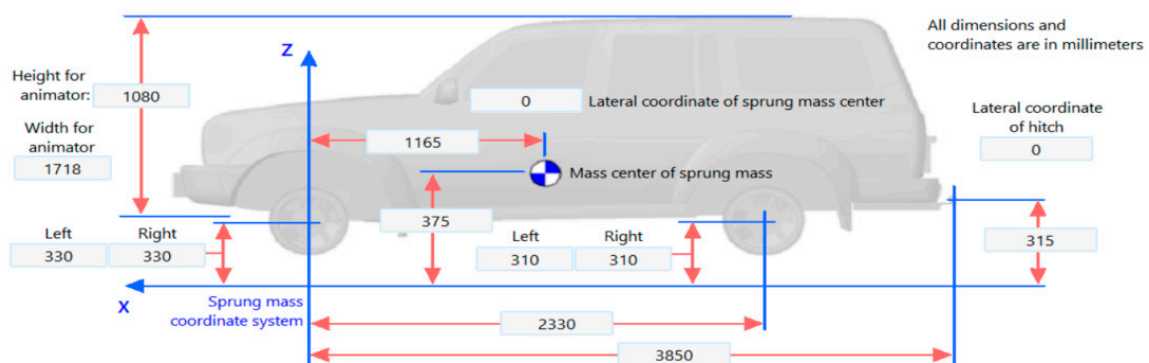
Figure 8. Body dimensions.

Table 1. Vehicle parameters.

Parameter	Value	Unit
Mass above suspension	1020	kg
Animator's canvas width	1718	mm
Inertia against yaw motion	1020	$Kg \cdot m^2$
Axle base	2330	mm
Wheel center elevation	310	mm
Elevation of the center of gravity	375	mm

The simulation conditions are specified when the entire vehicle's dimensions and parameter data have been configured in CarSim, and the CarSim parameter model is then transmitted to Simulink via an external interface. Currently, the route tracking joint simulation control model, which can perform joint simulation with input parameters, is made up of the Simulink control algorithm module and the CarSim parameter configuration module. Figure 9 displays the joint simulation control model for path tracking.
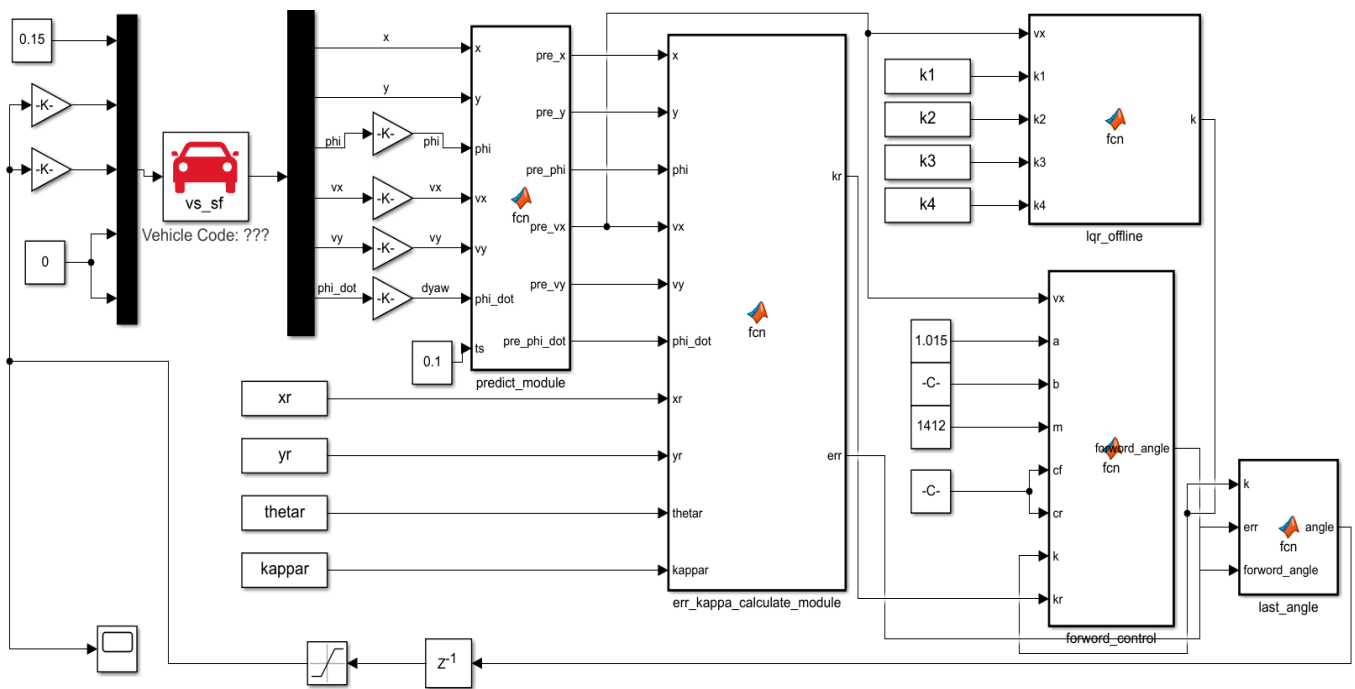
Figure 9. CarSim parameter configuration and Simulink algorithm module co-simulation platform.

Subsequently, a vehicle dynamics model based on the bicycle model is built, in order to validate the viability and path planning impact of the enhanced APF based on the safe distance protection model under the specified road conditions. The related constraint variables are set to minimize the objective cost function of the control commands under the constraints by linearizing and discretizing the model and creating the best objective function for controlling the path-tracking model. Through joint simulations in MATLAB, the embedded Simulink model, and CarSim, the main vehicle's active obstacle avoidance behavior is tested across various obstacle scenarios and various initial velocity parameters, to ensure the obtained active obstacle avoidance paths meet the actual vehicle's dynamics and kinematics, as well as the requirements for safety and stability.

6.3. Visual Analysis of Obstacle Avoidance Simulation in Different Obstacle Scenarios Before and After Optimization by Artificial Potential Field Method

6.3.1. Visual Analysis Before and After Optimization

In the comprehensive study shown in Figure 10, we comprehensively compared and analyzed the performance differences between the traditional Artificial Potential Field (APF) method and the optimized artificial potential field method in generating autonomous navigation paths and effectively avoiding obstacles. As an intuitive experimental comparison, this figure not only reveals the limitations and potential of the two methods in the field of vehicle path planning, but also clearly shows the path comparison before and after optimization, highlighting the significant advantages of the optimized APF algorithm.
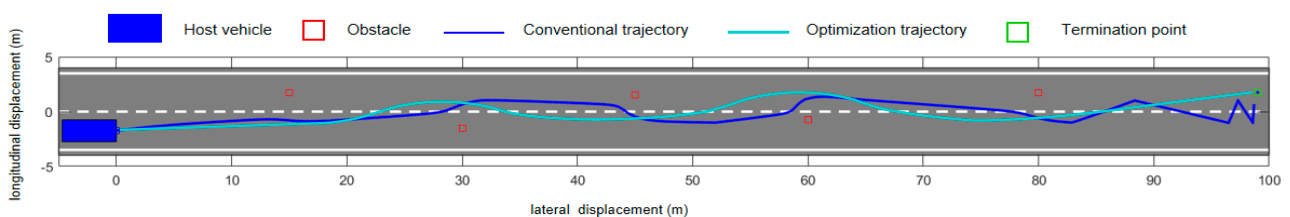

Figure 10. Comparison of obstacle avoidance trajectories of artificial potential field method before and after optimization.

In Figure 10, the defects of the traditional APF algorithm (depicted by the dark blue trajectory) are vividly revealed. When approaching the target area, the obstacle avoidance path of the intelligent vehicle continues to oscillate, falling into the so-called "local minimum trap", which makes the vehicle unable to reach the destination successfully even after multiple attempts. In addition, the path also has obvious shortcomings in safety, stability and smoothness. It is too close to the obstacle, which increases the risk of collision. Path instability, manifested as sudden changes in direction, may cause mechanical stress to the agent and threaten system reliability. Additionally, sharp turns and discontinuous movements along the path negatively affect the motion efficiency and energy consumption of the agent.

In contrast, the performance of the optimized APF algorithm (shown in light blue) is remarkable. It successfully generates a safe and stable path that guides the agent through a complex environment to reach the goal point efficiently and smoothly. The optimized path significantly improves its safety and maintains the safe distance between the agent and its obstacles. It enhances the path stability, avoids unnecessary direction mutation, and reduces the mechanical stress. At the same time, the smoothness of the path is optimized, sharp turns and discontinuous motion are avoided, the motion efficiency of the agent is improved, and energy consumption is reduced.

Through the intuitive comparison in Figure 10, we deeply understand the superiority of the optimized APF algorithm in the field of path planning, which not only solves the key limitations of traditional methods but also significantly improves the navigation ability of intelligent vehicles in complex environments, opening up new prospects for the development of autonomous navigation technology.

6.3.2. The Obstacle Avoidance Performance of the Algorithm Is Visually Verified in the Mixed Scene of Dynamic and Static Obstacles

As shown in Figure 11a, the yellow main vehicle is in the travel lane, beginning from the white starting point at a constant speed of 40 km/h. The blue vehicle is a stationary obstacle, located in the travel lane of the red obstacle vehicle with an initial speed of 20 km/h, and accelerating at 2.5 m/s². The yellow vehicle is located in the travel lane, when the vehicle visual detection and LiDAR feedback to the front of the blue stationary obstacle vehicle triggers the collision-avoidance system to improve the APF algorithm to make timely decisions, tracking the first section of the planned overtaking path to avoid the blue stationary obstacle vehicle, as shown in Figure 11b. At this time, when traveling to the overtaking lane, the vision and radar again feed back information about the existence of a slow-moving dynamic obstacle vehicle (red). At this time, the distance between the yellow vehicle and the red in front of it is lessening, once again triggering the collision-avoidance system to improve the APF algorithm, tracking the second section of the planned overtaking path to avoid the red dynamic obstacle vehicle 1 located in the overtaking lane, then returning to the traveling lane. As shown in Figure 11c, after passing the red obstacle vehicle 1 located in the overtaking lane, the scene detection system feeds back that there is another red dynamic obstacle vehicle in front of it, and that the vehicle is accelerating. The yellow main vehicle is still larger than the red obstacle vehicle in front of it, but the distance between them is shrinking, and, at this time, tracking the third section of the planned overtaking path to avoid the red dynamic obstacle vehicle 2, located in the traveling lane (Figure 11d), it finally successfully avoids all stationary and moving obstacle vehicles to successfully reach the target point. Compared with Figure 10 in Section 6.3, it is verified that the autonomous obstacle avoidance path planned by the optimized artificial potential field method and controlled by the DLQR tracking algorithm can meet the dynamics and kinematics requirements of the actual vehicle, and meet the requirements of steering safety, stability, and smoothness.
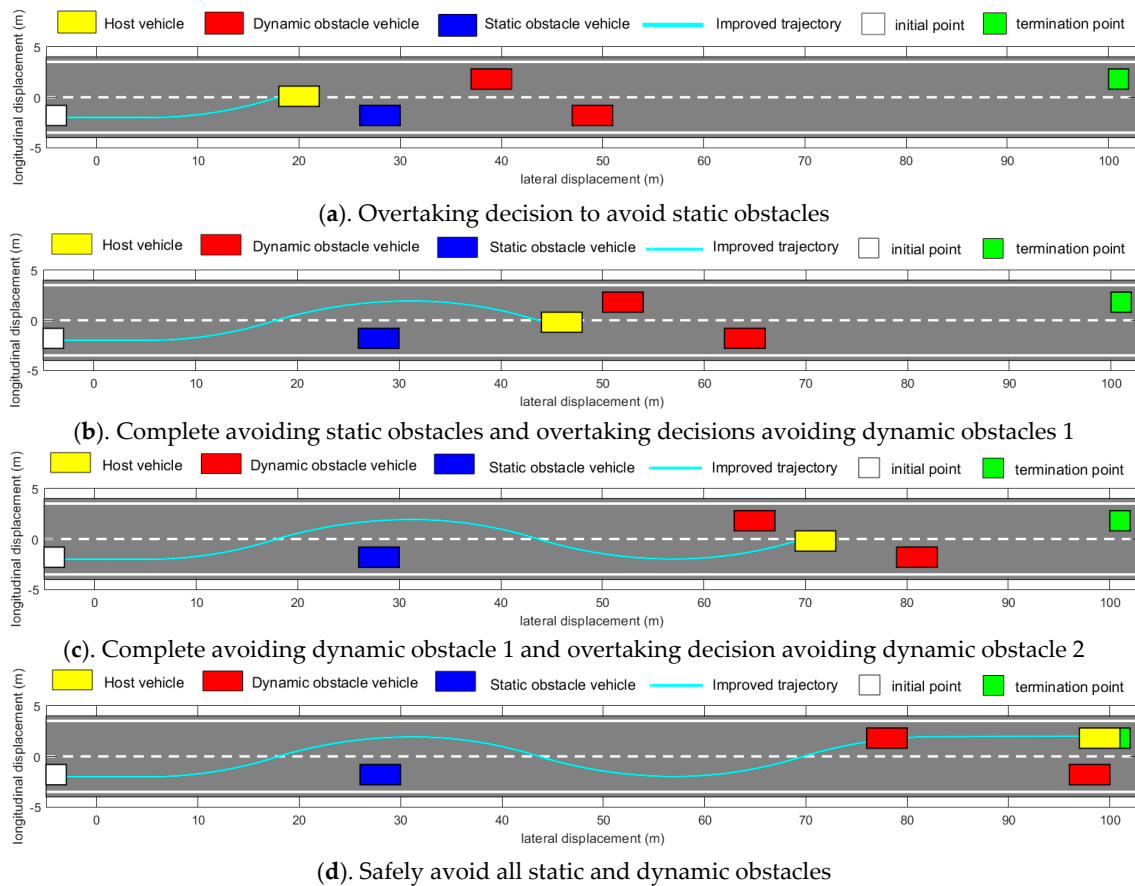
(**a**). Overtaking decision to avoid static obstacles

(**b**). Complete avoiding static obstacles and overtaking decisions avoiding dynamic obstacles 1

(**c**). Complete avoiding dynamic obstacle 1 and overtaking decision avoiding dynamic obstacle 2

(**d**). Safely avoid all static and dynamic obstacles

Figure 11. Simulation analysis of obstacle avoidance in different obstacle scenarios.

6.4. Simulation Data Analysis Before and After Optimization of Tracking Control Under Different Speed Parameters

When the discrete LQR algorithm is applied to lateral overtaking control, higher steering speeds may increase the risk of loss of control or sideslip of the vehicle during cornering. Fast steering maneuvers may lead to unstable vehicle maneuvers, especially at high speeds, where the system may over-respond or oscillate and thus lose stability, and the vehicle may also cause excessive impacts when executing overtaking maneuvers, due to the fact that, at high speeds, the inertia and dynamics of the vehicle may lead to greater lateral forces and accelerations, making the overtaking maneuvers more drastic and unstable. Overtaking control at high speeds requires more precise control of the system. Excessive speed may make it difficult for the controller to accurately track and adjust the position and trajectory of the vehicle. Overtaking needs to take into account the position, speed, and acceleration of the vehicle in front of it to ensure that the overtaking maneuver is completed safely. Excessive speed may make overtaking more dangerous and increase the risk of collision with other vehicles.

Therefore, when applying the discrete LQR algorithm to lateral-overtaking control, the dynamic tracking control performance of the system needs to be verified at different speeds, balancing the relationship between speed parameters and system stability, and appropriately selecting the appropriate speed range to ensure the stability and safety of the lateral overtaking operation. Through the joint simulation of the CarSim parameter configuration and the Simulink algorithm control module, the DLQR algorithm based on different initial speeds is implemented to track the obstacle avoidance trajectory planned in different visual scenes before and after the above optimization. The simulation and data comparisons of vehicle steering angle, vehicle yaw angle, and vertical steering forces of front and rear wheels over time were obtained under different speeds before and after optimization. This analysis assesses whether the lateral control of the vehicle can meet the requirements of the actual vehicle dynamics and kinematics, as well as the necessary standards for steering safety and stability.

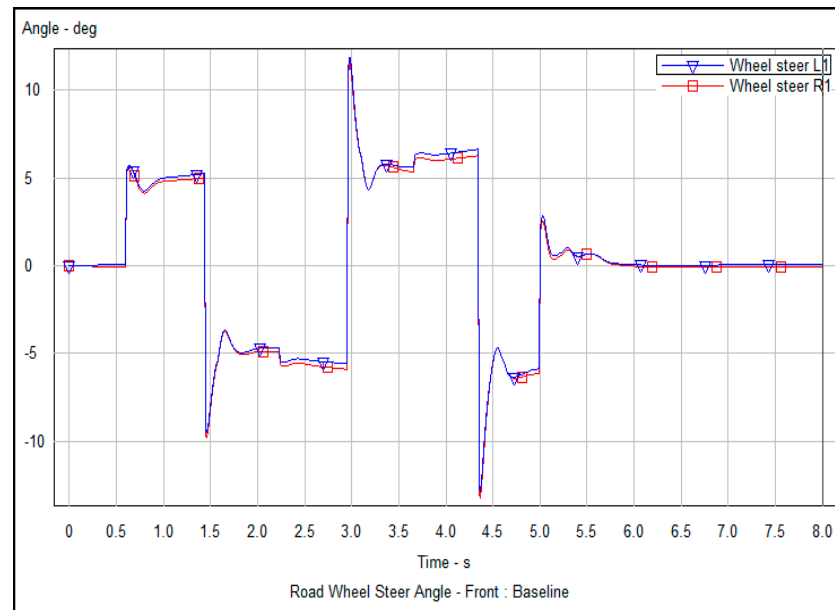6.4.1. Comparison of Experimental Values Before and After Vehicle Lateral Steering Angle Optimization

Vehicle lateral steering angle optimization refers to changing the lateral movement of the vehicle by changing the lateral steering angle of the front wheel when overtaking to avoid obstacles, which can reflect the stability and controllability of the vehicle-tracking controller in ensuring that the vehicle can smoothly and safely travel along the planned trajectory. Figures 12a–c and 13a–c show the numerical analysis of the variation of the lateral steering angle of the vehicle over time, before and after optimization, respectively, obtained from the vehicle tracking controller's driving experiment along the planned obstacle avoidance trajectory at speeds of 40, 50 and 60 km/h.

The comparison of experimental values before and after optimizing the lateral steering angle is shown in Table 2. By comparing the data in Figure 12a–c with those in Figure 13a–c, it is evident that the variation amplitude of the lateral angle of the controller vehicle after optimization is smaller than that of the vehicle before optimization, and the tracking and control performance of the reference path is improved at different speeds. Under the three speed conditions, the fluctuation range of both maximum steering angle and steering angle change rate is reduced after optimization, with the angle change range at 60 km/h being smaller than at 40 and 50 km/h. The lateral control of the vehicle shows improved lane-changing performance. The variation amplitude of the optimized lateral angle data demonstrates that the lateral control performance of the vehicle is better during lane change and overtaking. The optimized controller enables the vehicle to turn to the corresponding angle more quickly, without delay and hysteresis. The vehicle can achieve a small steering radius and greater stability during the steering process, so that the vehicle can maintain stability and avoid sideslipping, loss of control, or instability. Consequently, the optimized vehicle tracking controller provides better grip and handling stability during high-speed or sharp turns and lane changes, speeding and tightening rotation and improving the vehicle's maneuverability.
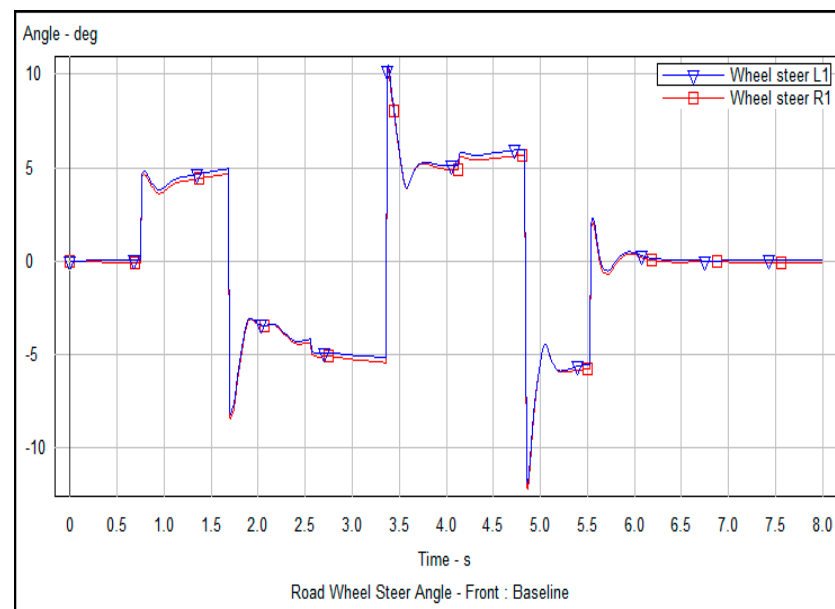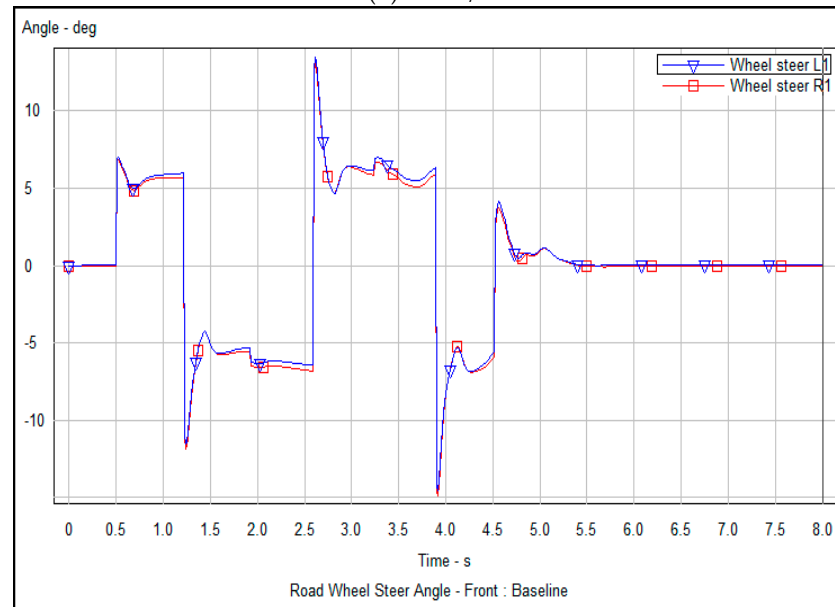

(**a**) 40 km/h
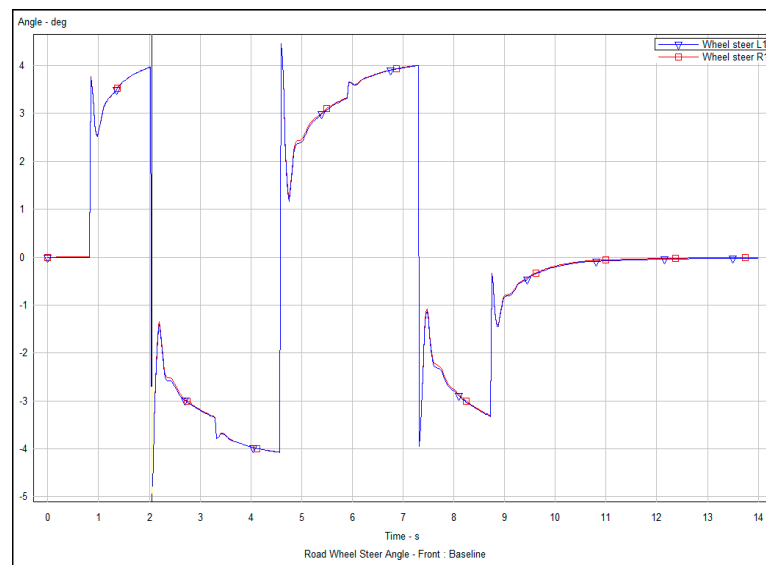
Figure 12. *Cont.*
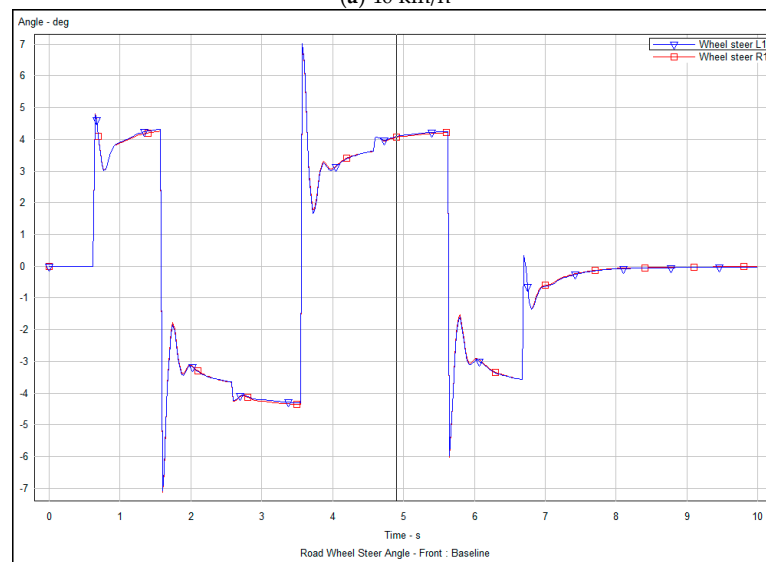
(**b**) 50 km/h

(**c**) 60 km/h

Figure 12. The results of lateral angle data of vehicle before optimization.

Table 2. Comparison of experimental values before and after vehicle lateral steering angle optimization.
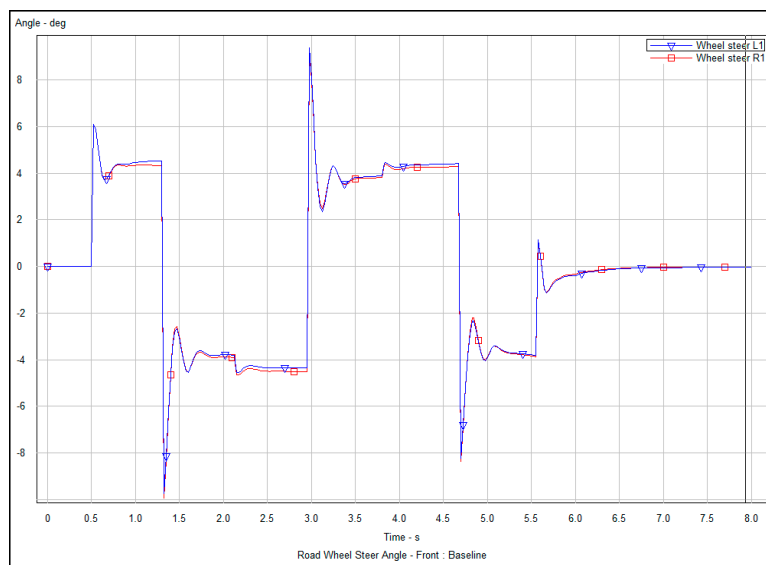
	Traditional Artificial Potential Field Method		Optimized Artificial Potential Field Method	
Speed (km/h)	Peak Steering Angle Required for Lateral Movement of Vehicle (deg)	Fluctuation Range of Steering Angle Required for Lateral Movement of Vehicle (deg)	Peak Steering Angle Required for Lateral Movement of Vehicle (deg)	Fluctuation Range of Steering Angle Required for Lateral Movement of Vehicle (deg)
40	11°	0~7°	5°	0~3°
50	13°	0~9°	7°	0~5°
60	15°	0~11°	10°	0~7°

(**a**) 40 km/h

(**b**) 50 km/h

(**c**) 60 km/h

Figure 13. The results of lateral angle data of vehicle after optimization.

6.4.2. Vehicle Lateral Slippage Angle Optimization Before and After Comparison

The lateral sideslip angle refers to the angle between the vehicle's actual driving direction and the center line of its driving track during lateral movements, such as overtaking or avoiding obstacles. This angle is an important index to measure the lateral dynamic stability of the vehicle. An excessive sideslip angle may cause the vehicle to lose control and compromise safety. Figures 14a–c and 15a–c show the numerical analysis, before and after optimization, respectively, of the lateral slip angle of the vehicle obtained through the experimental simulation.

The comparative experimental values of the vehicle's lateral slip angle, before and after optimization, are shown in Table 3. By comparing the data in Figure 14a–c with those in Figure 15a–c, it can be seen that under different speed conditions, after optimization, the peak and duration of the sideslip the angle are reduced, the fluctuation amplitude of the sideslip angle's change rate is small, the range of variation is more reasonable, and the tracking controller has stable lateral control performance. The results show that the vehicle can maintain a stable side yaw angle, and the side yaw angle and jitter fluctuation are small, indicating that the vehicle has excellent stability and can keep on the expected trajectory. The vehicle is able to respond quickly to steering wheel control inputs, producing corresponding side-angle changes to achieve accurate maneuvering and directionality. The vehicle is better able to quickly return to a stable side angle, and when the vehicle encounters crosswinds, uneven roads, or unexpected situations, it should be able to recover quickly and maintain stable side control.
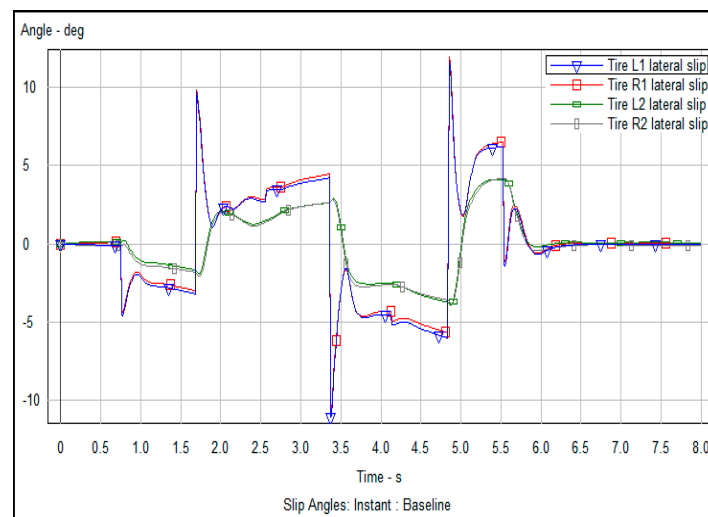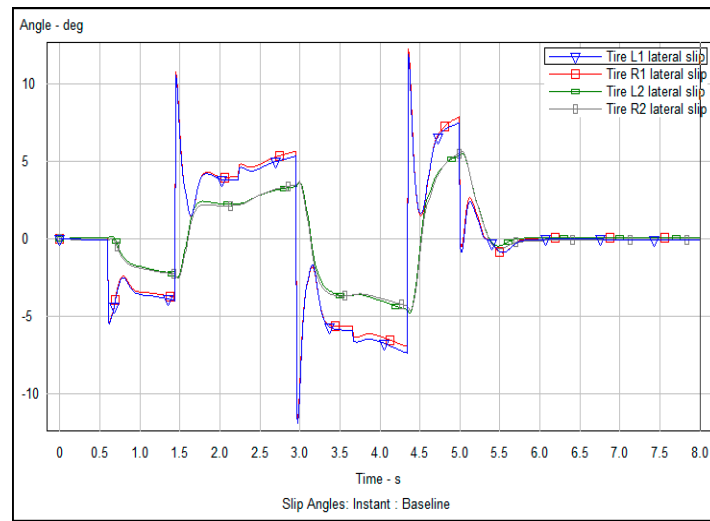

(**a**) 40 km/h
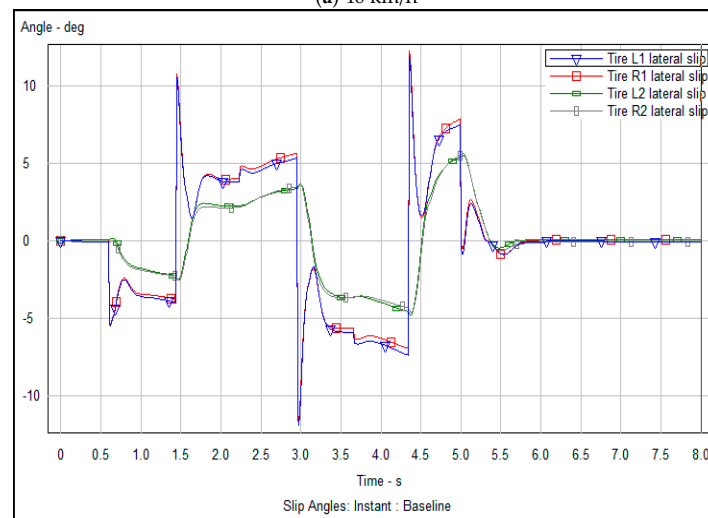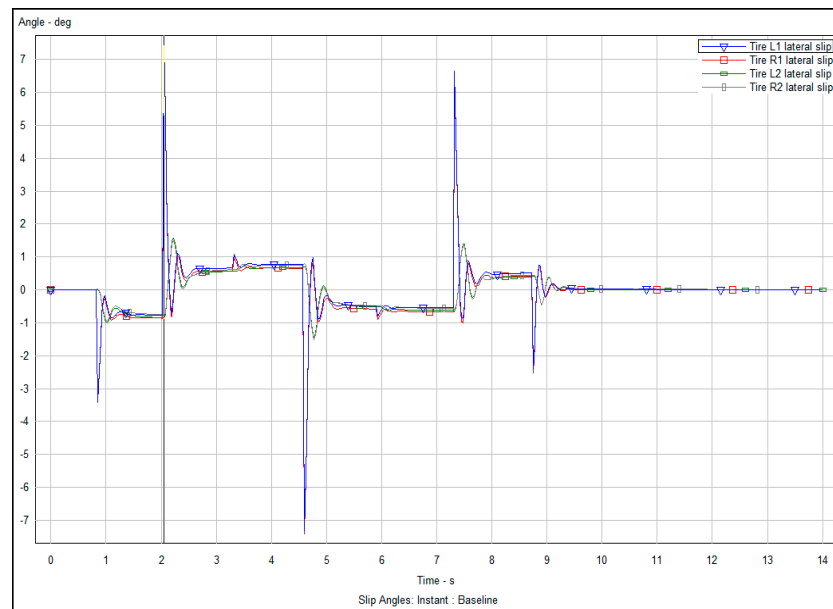

(**b**) 50 km/h

Figure 14. *Cont.*

(**c**) 60 km/h

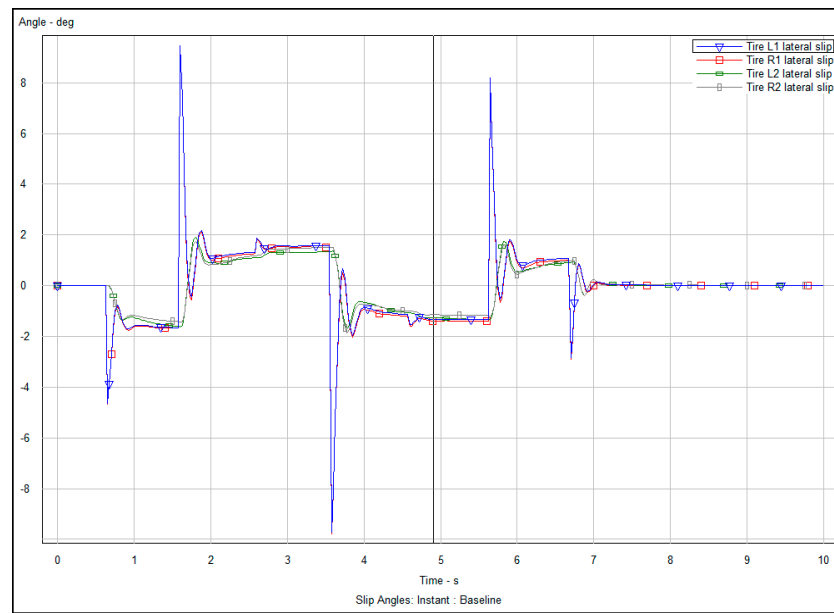**Figure 14.** Vehicle lateral slip angle data before optimization.

Table 3. Comparison of experimental values before and after vehicle lateral slippage angle optimization.

Speed (km/h)	Traditional Artificial Potential Field Method		Optimized Artificial Potential Field Method	
	The Peak of the Sideslip Angle in the Lateral Movement of Vehicle (deg)	Fluctuation Range of Sideslip Angle During Lateral Movement of Vehicle (deg)	The Peak of the Sideslip Angle in the Lateral Movement of Vehicle (deg)	Fluctuation Range of Sideslip Angle During Lateral Movement of Vehicle (deg)
40	12°	0~12°	7°	0~6°
50	13°	0~13°	9°	0~8°
60	14°	0~14°	11°	0~10°

(**a**) 40 km/h

Figure 15. *Cont.*

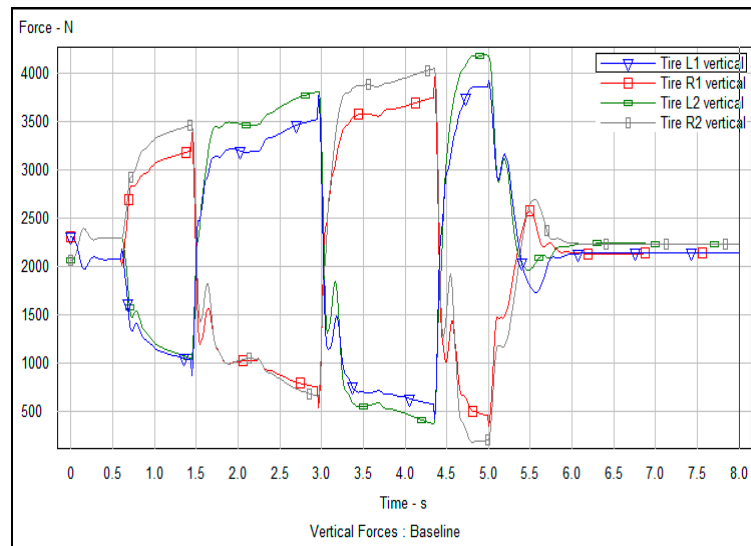(**b**) 50 km/h
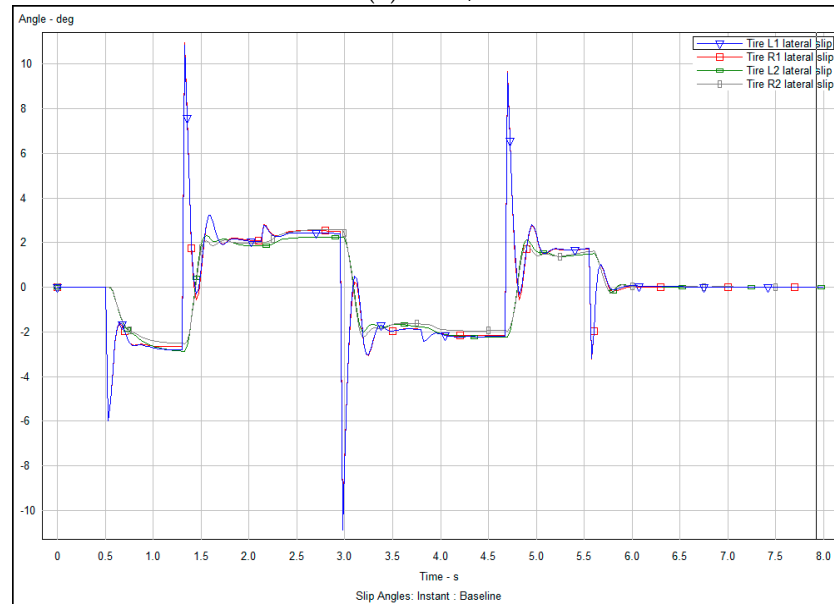
(**c**) 60 km/h

Figure 15. Vehicle lateral slip angle data following optimization.

6.4.3. Numerical Comparison of the Pre- and Post-Optimization of Vertical Support Force of Front- and Rear-Wheel Steering
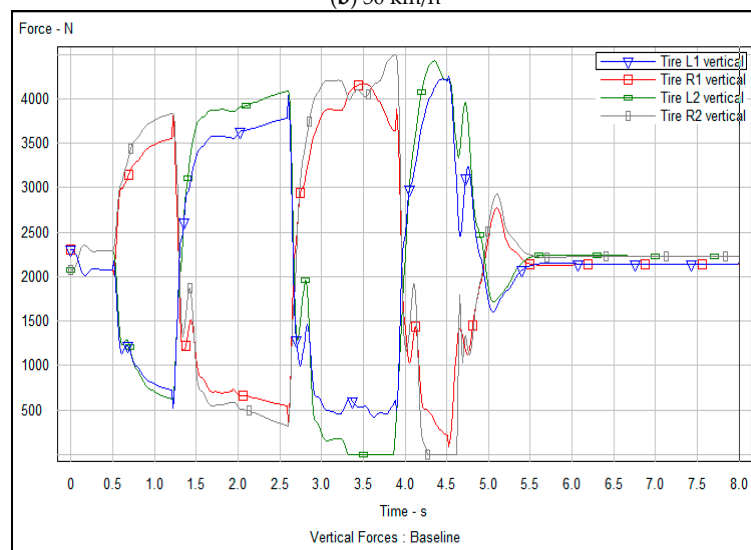
The vertical supporting force of the front and rear wheels of a vehicle refers to the force perpendicular to the ground caused by the ground reaction force in the process of transverse movements such as lane changing and overtaking. This force is critical for maintaining the stability and handling of the vehicle. Figures 16a–c and 17a–c present analyses of vertical support force of the front and rear wheels of the vehicle through experimental simulation, before and after optimization, respectively.
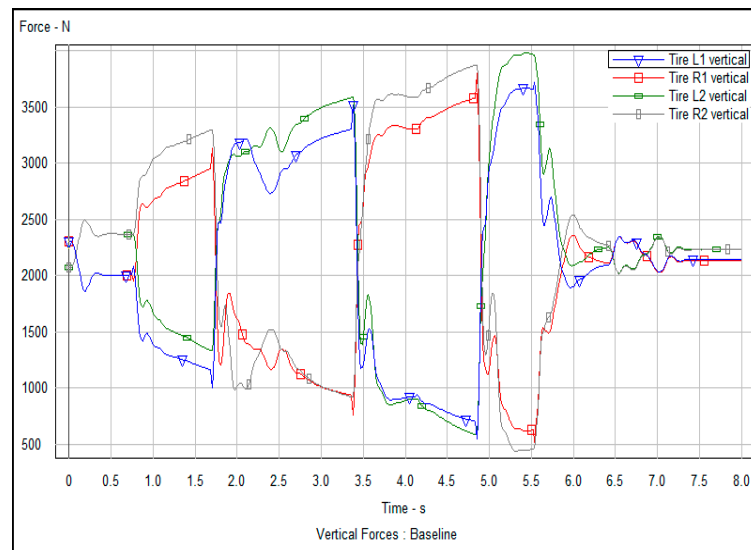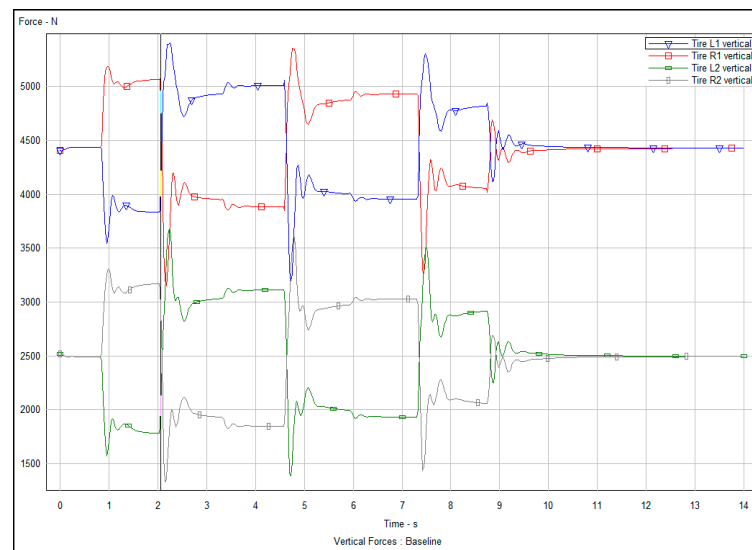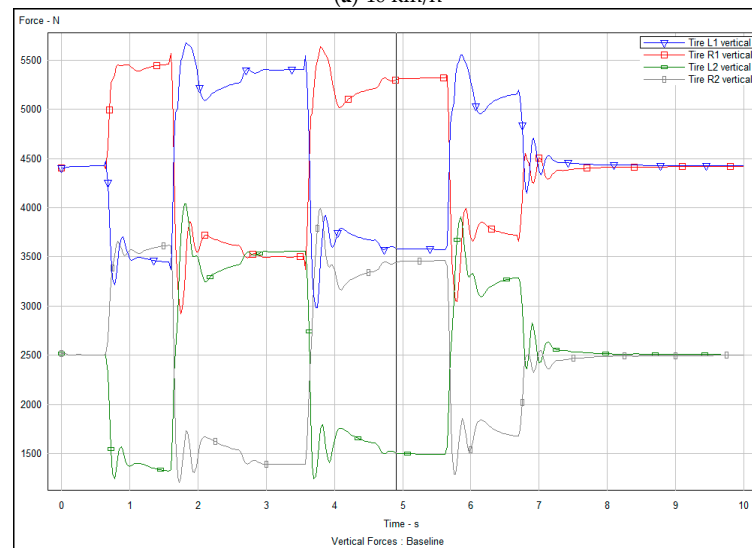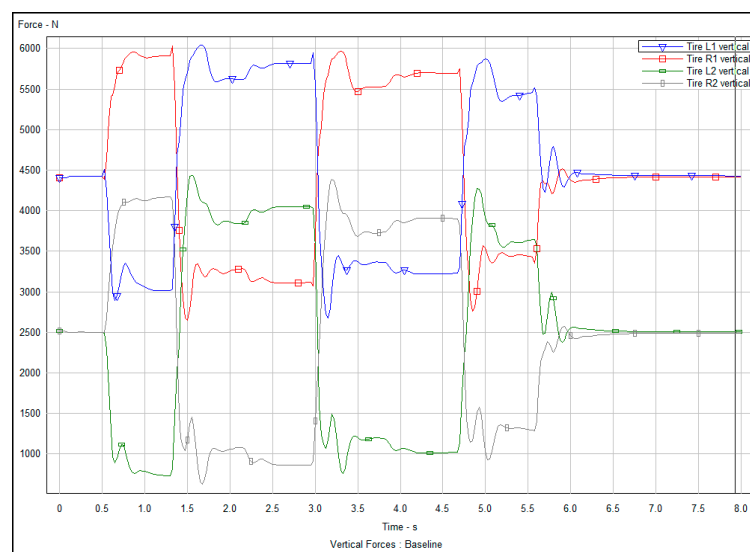
(**a**) 40 km/h

(**b**) 50 km/h

(**c**) 60 km/h

Figure 16. Numerical analysis of the vertical support force data of the front and rear wheels of the vehicle before optimization.

(**a**) 40 km/h

(**b**) 50 km/h

(**c**) 60 km/h

Figure 17. Numerical analysis of the vertical support force data of the front and rear wheels of the vehicle after optimization.

The results of optimizing the vertical support force data of front and rear four-wheel steering are shown in Table 4. As shown in the numerical comparison between Figures 16a–c and 17a–c, under different speed conditions, the optimized tracking controller shows better lateral control performance than the pre-optimized tracking controller in terms of the numerical size and uniform distribution of the steering vertical support force of the vehicle's four wheels. When the vehicle encounters an obstacle, the algorithm effectively enables collision avoidance and lane-change/overtaking control, and the four wheels of the vehicle maintain better ground pressure, increase the support force of the inner wheel, and reduce the support force of the outer wheel. This can provide higher lateral acceleration and better maneuvering performance, achieve effective turning and maneuvering control and cornering characteristics, and ensure optimal grip and handling stability, which results in faster turning speeds and more precise handling responses. When the vehicle encounters crosswinds, uneven road surfaces, or other disturbances, it can also adjust the vertical wheel steering support and wheel support distribution to maintain stability and avoid loss of control or skidding.

Table 4. Optimizing the vertical support force of front- and rear-wheel steering.

Speed (km/h)	Traditional Artificial Potential Field Method		Optimized Artificial Potential Field Method	
	Peak Vertical Support Force of Front and Rear Wheels in Lateral Movement of Vehicle (N)	Lower Limit of Vertical Support Force Fluctuation of Front and Rear Wheels in Lateral Movement of Vehicle (N)	Peak Vertical Support Force of Front and Rear Wheels in Lateral Movement of Vehicle (N)	Lower Limit of Vertical Support Force Fluctuation of Front and Rear Wheels in Lateral Movement of Vehicle (N)
40	4100	400	5100	1400
50	4300	200	5600	1300
60	4500	0	6050	950

In summary, insufficient steering speed may result in slow steering response, while excessive steering speed may reduce control accuracy. Appropriate steering speed can provide better maneuvering performance, and turning at the appropriate steering speed helps the vehicle more easily track the planned path and receive adequate feedback. Comparison of experimental parameters in Table 2 shows that the values of lateral control steering angle and side deflection angle across three speed conditions fluctuate within a reasonable range. The controller effectively maintains stable path tracking under various reasonable steering speed parameters, ensuring the vehicle's stability while driving. Additionally, the vertical support forces of the front and rear tires are sufficient to meet the requirements of safe lane changes and collision avoidance during overtaking at higher speeds, demonstrating the controller's high tracking precision, adaptability, and resilience.

7. Conclusions

The integration of artificial intelligence in autonomous driving marks a pivotal phase in automotive evolution. However, fully replacing human drivers remains challenging due to critical safety and reliability concerns. Our research advances autonomous vehicle path planning and tracking control through an enhanced Artificial Potential Field (APF) method. By addressing the APF's limitations in target reachability and local optimum issues, and by integrating safety distance models and dynamic road-repulsive potential fields, we enhance the precision of path planning. Additionally, a linearized and discretized vehicle dynamics model enables optimal path tracking under constraints, minimizing control costs. Simulation results using MATLAB/Simulink and CarSim demonstrate reduced steering and sideslip angles (by 5 to 10° and 3 to 5°, respectively), and increased vertical support forces (from 1000 to 1450 N), showcasing our algorithm's superior obstacle avoidance and lane-changing capabilities under dynamic conditions. The DLQR algorithm controller's performance, maintaining parameters within rational boundaries, highlights its robustness in dynamic obstacle environments.

Future directions in research involve integrating multi-sensor technologies and real-world testing to refine obstacle avoidance algorithms, aiming for enhanced accuracy and robustness in complex, real-world scenarios. Path planning and tracking control, when seamlessly integrated, ensure vehicle stability, comfort, and effective obstacle navigation. Our vision includes advanced testing environments and real-world vehicle trials to rigorously evaluate algorithmic innovations in practical driving contexts, bridging simulation success and real-world complexities.

Author Contributions: Conceptualization, C.Z. and Z.C.; methodology, C.Z.; software, Z.C.; validation, Z.C., X.L. and T.Z.; formal analysis, X.L.; investigation, T.Z.; resources, C.Z.; data curation, Z.C.; writing—original draft preparation, Z.C.; writing—review and editing, C.Z.; visualization, X.L.; supervision, T.Z.; project administration, Z.C.; funding acquisition, C.Z. All authors have read and agreed to the published version of the manuscript.

Data Availability Statement: The original contributions presented in the study are included in the article, further inquiries can be directed to the corresponding author.

Conflicts of Interest: The authors declare no conflict of interest.

References

1. Xu, X.; Hu, W.; Dong, H.; Wang, Y.; Xiao, L.Y.; Li, P.H. Review of key technologies for autonomous vehicle test scenario construction. *Automot. Eng.* **2021**, *43*, 610–619.
2. Dudziak, A.; Stoma, M.; Kuranc, A.; Caban, J. Assessment of Social Acceptance for Autonomous Vehicles in Southeastern Poland. *Energies* **2021**, *14*, 5778. [CrossRef]
3. Hwang, M.H.; Lee, G.S.; Kim, E.; Kim, H.W.; Yoon, S.; Talluri, T.; Cha, H.R. Regenerative braking control strategy based on AI algorithm to improve driving comfort of autonomous vehicles. *Appl. Sci.* **2023**, *13*, 946. [CrossRef]
4. Nelson, S.P. *Challenges and Technologies: The Human Friendly Vehicle in 2030 and Beyond*; Freescale Semiconductor, Inc.: Mansfield, TX, USA, 2009.
5. Fagnant, D.J.; Kockelman, K. Preparing a nation for autonomous vehicles: Opportunities, barriers and policy recommendations. *Transp. Res. Part A Policy Pract.* **2015**, *77*, 167–181. [CrossRef]
6. Folsom, T.C. Social ramifications of autonomous urban land vehicles. In Proceedings of the 2011 IEEE International Symposium on Technology and Society (ISTAS), Chicago, IL, USA, 23–25 May 2011; pp. 1–6.
7. Millard-Ball, A. Pedestrians, autonomous vehicles, and cities. *J. Plan. Educ. Res.* **2018**, *38*, 6–12. [CrossRef]
8. Xu, Z.; Zhang, K.; Min, H.; Wang, Z.; Zhao, X.; Liu, P. What drives people to accept automated vehicles? Findings from a field experiment. *Transp. Res. Part C Emerg. Technol.* **2018**, *95*, 320–334. [CrossRef]
9. Le Vine, S.; Zolfaghari, A.; Polak, J. Autonomous cars: The tension between occupant experience and intersection capacity. *Transp. Res. Part C Emerg. Technol.* **2015**, *52*, 1–14. [CrossRef]
10. Chen, L.; Liu, C.; Shi, H.; Gao, B. New robot planning algorithm based on improved artificial potential field. In Proceedings of the 2013 Third International Conference on Instrumentation, Measurement, Computer, Communication and Control, Shenyang, China, 21–23 September 2013; pp. 228–232.
11. Tang, Z.; Ji, J.; Wu, M.; Fang, J.C.; Chen, M.Z. Vehicles path planning and tracking based on an improved artificial potential field method. *J. Southwest Univ. Nat. Sci. Ed.* **2018**, *40*, 174–182.
12. An, L.-F.; Chen, T.; Cheng, A.-G.; Fang, W. Simulation on the path planning of intelligent vehicles based on artificial potential field algorithm. *Automot. Eng.* **2017**, *39*, 1451–1456.
13. Xiu, C.; Hui, C. A research on local path planning for autonomous vehicles based on improved APF method. *Automot. Eng.* **2013**, *35*, 808–811.
14. Lee, J.; Nam, Y.; Hong, S. Random force based algorithm for local minima escape of potential field method. In Proceedings of the 2010 11th International Conference on Control Automation Robotics & Vision, Singapore, 7–10 December 2010; pp. 827–832.
15. Song, X.; Pan, L.; Cao, H. Local path planning for vehicle obstacle avoidance based on improved intelligent water drops algorithm. *Automot. Eng.* **2016**, *38*, 185–191.
16. Wang, X.; Liu, M.; Ci, Y.; Yang, Y. Effectiveness of driver's bounded rationality and speed guidance on fuel-saving and emissions-reducing at a signalized intersection. *J. Clean. Prod.* **2021**, *325*, 129343. [CrossRef]
17. Jianhua, L.; Jianguo, Y.; Huaping, L.; Peng, G.; Meng, G. Robot global path planning based on ant colony optimization with artificial potential field. *Nongye Jixie Xuebao/Trans. Chin. Soc. Agric. Mach.* **2015**, *46*, 18–27.

18. Liu, Y.; Zhang, W.-G.; Li, G.-W. Study on path planning based on improved PRM method. *Jisuanji Yingyong Yanjiu* **2012**, *29*, 63628171.

19. Zheng, Y.; Shao, X.; Chen, Z.; Zhang, J. Improvements on the virtual obstacle method. *Int. J. Adv. Robot. Syst.* **2020**, *17*, 1729881420911763. [CrossRef]

20. Matoui, F.; Boussaid, B.; Abdelkrim, M.N. Distributed path planning of a multi-robot system based on the neighborhood artificial potential field approach. *Simulation* **2019**, *95*, 637–657. [CrossRef]

21. Yue, M.; Ning, Y.; Guo, L.; Zhao, J. A WIP vehicle control method based on improved artificial potential field subject to multi-obstacle environment. *Inf. Technol. Control* **2020**, *49*, 320–334. [CrossRef]

22. Zhang, L.X.; Wu, G.Q.; Guo, X.X. Path Tracking Using Linear Time varying Model Predictive Control for Autonomous Vehicle. *J. Tongji Univ. Nat. Sci.* **2016**, *44*, 1595–1603.

23. Chang, L.T.; Tao, H.J.; Lei, G.L.; Guang, L.X.; Ping, B.X. Agricultural machine path tracking method based on fuzzy adaptive pure pursuit model. *Nongye Jixie Xuebao = Trans. Chin. Soc. Agric. Mach.* **2013**, *44*, 205–210.

24. Lee, S.-H.; Lee, Y.O.; Kim, B.-A.; Chung, C.C. Proximate model predictive control strategy for autonomous vehicle lateral control. In Proceedings of the 2012 American control conference (ACC), Montreal, QC, Canada, 27–29 June 2012; pp. 3605–3610.

25. Zhou, L.H.; Shi, P.L.; Jiang, J.X. Simulation research on vehicle stability control based on collision avoidance trajectory tracking. *J. Shandong Univ. Technol. (Nat. Sci. Ed.)* **2021**, *35*, 75–81.

26. Wu, L.; Ci, Y.; Sun, Y.; Qi, W. Research on Joint Control of On-ramp Metering and Mainline Speed Guidance in the Urban Expressway based on MPC and Connected V ehicles. *J. Adv. Transp.* **2020**, *2020*, 7518087. [CrossRef]

27. Morales, S.; Magallanes, J.; Delgado, C.; Canahuire, R. LQR trajectory tracking control of an omnidirectional wheeled mobile robot. In Proceedings of the 2018 IEEE 2nd Colombian Conference on Robotics and Automation (CCRA), Barranquilla, Colombia, 1–3 November 2018; pp. 1–5.

28. Chen, J.; Li, L.; Song, J. A study on vehicle stability control based on LTV-MPC. *Automot. Eng.* **2016**, *38*, 308–316.

29. Schildbach, G.; Borrelli, F. Scenario model predictive control for lane change assistance on highways. In Proceedings of the 2015 IEEE Intelligent Vehicles Symposium (IV), Seoul, Republic of Korea, 28 June–1 July 2015; pp. 611–616.

30. Carvalho, A.; Gao, Y.; Lefevre, S.; Borrelli, F. Stochastic predictive control of autonomous vehicles in uncertain environments. In Proceedings of the 12th International Symposium on Advanced Vehicle Control, Tokyo, Japan, 22–26 September 2014.

31. Carvalho, A.; Lefévre, S.; Schildbach, G.; Kong, J.; Borrelli, F. Automated driving: The role of forecasts and uncertainty—A control perspective. *Eur. J. Control* **2015**, *24*, 14–32. [CrossRef]

32. Gao, Y.; Gray, A.; Tseng, H.E.; Borrelli, F. A tube-based robust nonlinear predictive control approach to semiautonomous ground vehicles. *Veh. Syst. Dyn.* **2014**, *52*, 802–823. [CrossRef]

33. Gao, Y.; Lin, T.; Borrelli, F.; Tseng, E.; Hrovat, D. Predictive control of autonomous ground vehicles with obstacle avoidance on slippery roads. In Proceedings of the Dynamic Systems and Control Conference, Cambridge, MA, USA, 12–15 September 2010; pp. 265–272.

34. Ji, J.; Ji, P.; Peng, H. Design of 3D virtual dangerous potential field for vehicle active collision avoidance. *Automot. Eng. Mag.* **2016**, *38*, 1065–1071.

35. Ji, J.; Khajepour, A.; Melek, W.W.; Huang, Y. Path planning and tracking for vehicle collision avoidance based on model predictive control with multiconstraints. *IEEE Trans. Veh. Technol.* **2016**, *66*, 952–964. [CrossRef]

36. Zhang, Z.; Zheng, L.; Li, Y.; Zeng, P.; Liang, Y. Structured road-oriented motion planning and tracking framework for active collision avoidance of autonomous vehicles. *Sci. China Technol. Sci.* **2021**, *64*, 2427–2440. [CrossRef]

37. Chen, T.; Zhang, P.; Gao, S.; Zhang, Q. Research on the dynamic target distribution path planning in logistics system based on improved artificial potential field method-fish swarm algorithm. In Proceedings of the 2018 Chinese Control and Decision Conference (CCDC), Shenyang, China, 9–11 June 2018; pp. 4388–4391.